Synchronous Measuring Techniques in Parallel to MRE:

Study of Pressure, Pre-Tension, and Surface Dynamics

BY

SPENCER THOMAS BRINKER
B.S. (Southern Illinois University Edwardsville) 2009

THESIS

Submitted as partial fulfillment of the requirements
for the degree of Doctor of Philosophy of Mechanical Engineering
in the Graduate College of the
University of Illinois at Chicago, 2016

Chicago, Illinois

Defense Committee:

Dieter Klatt, Chair and Advisor
Thomas J. Royston, Bioengineering
Michael J. Scott, Mechanical and Industrial Engineering
Richard L. Magin, Bioengineering
Marvin A. Rossi, Rush Epilepsy Center

To my parents,
David and Leslie Brinker

ACKNOWLEDGMENTS

From the year 2010 until 2016, there are several people to whom I owe great amounts of thanks to for their help and support. Thank to my mother and father for believing in me from the beginning to the end that I could accomplish this undertaking at UIC. And also to the rest of my family and close friends who kept my life outside of school in good times and happiness. It gave me great comfort through this entire experience knowing everyone was behind me.

I enormously thank Thomas J. Royston, Richard L. Magin, Michael J. Scott for giving me a chance at UIC. I thank them for their willingness to personally engage with me during my times of trial getting started in academia. And I must thank Marvin A. Rossi for initially providing me with an opportunity and place to gain interest in human brain applications.

I must also speak of and thank several individuals whose insight and work made portions of the work in this dissertation possible. I like to name Lukasz Zientara, Eric Schmidt**,** David Mecha, Thomas Bruzan, and Matthew Schuck, and Weiguo Li for all their support in helping me with experimentation development. To all my lab mates Kaya Yasar, Dave Burns, Altaf Khan, Yifei Liu, Zoujun Dai, Ying Peng, Allen Ye, Benjamin Schwartz, and Ziying Yin for their insight and support in my dissertation work. And mostly I thank Steve Kearney for his support and partnerships in many of the projects we performed together at UIC.

Dieter Klatt is a true friend, which has been an invaluable experience for me. I am proud and thankful to say he is my PhD advisor. His positive support inside and outside of the job has allowed me to explore my academic research interests to the fullest. I have learned many disciplines in writing, research, and theory from Dieter that I will carry into my future career.

Plainly and simply, getting through this six year period at times was challenging. Several instances of uneasy examinations, projects, experiments, or situations of uncertainty left me with trial or

worry. However, certain beliefs I have allowed me many times to lay my head down at night in peace. I always found considerable rest, hope, and patience regarding any challenges by engaging in my belief that there is a spiritual existence of Jesus Christ and practicing his teachings. For me, this is the most significant acknowledgment I owe.

STB

Chapter 4 of this dissertation represents a conference presentation (Brinker SB, Kearney SP, Royston TJ, Klatt D. Effects of quasistatic internal pressure loads on a multi-layered pressure vessel phantom in MR elastography. Proceedings of ICEM: 16th International Conference on Experimental Mechanics, Cambridge, UK, July 7 – 11, 2014). Chapter 5 contains a series of unpublished experiments that are an extension of the work from Chapter 4 and will potentially be published in an additional manuscript. The material in Chapter 6 is under review for publication in the Journal of Mechanical Behavior of Biomedical Materials. Portions of Chapter 7 are under review for presentation at the 15th International Tissue Elastography Conference, Fairlee, Vermont, October 16 – 19th, 2016. Dieter Klatt, Steve Kearney, and Thomas J. Royston will be included as co-authors in some of these publications for contributions regarding image and acoustic analysis.

TABLE OF CONTENTS

CHAPTER			PAGE
1	INTRODUCTION		1
	1.1	Motivation	1
	1.2	Synthetic Materials for Mimicking Soft Biological Tissue	2
	1.3	A Brief Historical-Based Overview of MRI	2
	1.4	Magnetic Resonance Elastography	4
	1.5	MRE Data Collection	4
2	THEORY AND DATA PROCESSING		9
	2.1	Wave Equation and Inversion Methods	9
	2.2	MRE Data Processing	13
	2.3	Tensile Testing and Hyperelastic Theory	14
	2.4	SLDV and Line Profile Curve Fitting	16
3	ELASTIC PHANTOMS AND SPECIMENS		19
	3.1	Ecoflex and Plastisol Preparation	19
	3.2	Pressure Loaded Phantom	21
	3.3	Tensile Specimen	22
	3.4	Optical Validation Cylindrical Specimens	23
4	EFFECTS OF QUASISTATIC INTERNAL PRESSURE LOADS ON A MULTI-LAYERED PRESSURE VESSEL PHANTOM IN MRE		25
	4.1	Introduction	25
	4.2	Materials and Methods	27
	4.3	Results and Discussion	31
5	CONSTRUCTION OF AN INTERCONNECTED POROSITY PHANTOM FOR STUDYING PRESSURE LOADING IN POROUS MEDIA WITH MRE		37
	5.1	Introduction	37
	5.2	Interconnected Porosity Phantom Design and Construction	38
	5.3	Image Analysis	39
6	DEMONSTRATION OF CONCURRENT TENSILE TESTING AND MAGNETIC RESONANCE ELASTOGRAPHY		42
	6.1	Introduction	42
	6.2	Materials and Methods	44
	6.3	Results	50
	6.4	Discussion	55

TABLE OF CONTENTS (continued)

CHAPTER PAGE

7 RELATING DYNAMIC SURFACE AND INTERNAL DISPLACEMENT FIELDS IN SOFT TISSUE-MIMICKING MEDIA: SYNCHRONOUS ACQUISITION OF MRE AND SLDV 61
7.1 Introduction 61
7.2 Materials and Methods 63
7.3 Results and Discussion 67

8 CONCLUSION 78

CITED LITERATURE 80

VITA 84

LIST OF TABLES

TABLE		PAGE
TABLE I	CALCULATED MECHANICAL PROPERTIES LIST	9
TABLE II	TIMELINE OF SHEAR MODULUS FOR MULTILAYER PHANTOM OVER 4 PRESSURE CYCLES	33
TABLE III	MRE SHEAR STORAGE MODULUS AND TENSILE STRESS FOR ALL STRAINS	54
TABLE IV	TENSILE STRESS AND SHEAR STORAGE MODULUS CORRELATION	55
TABLE V	MATERIALS USED IN TENSILE-MRE PROBE	60
TABLE VI	COMPLEX SHEAR MODULUS COMPARISON BETWEEN MRE AND OE	73

LIST OF FIGURES

FIGURE PAGE

Figure 2-1: (a) Magnitude image of axial slice with red dotted line representing masked out ROI. (b) Snapshot of wave propagation with displacement perpendicular to imagine plane. (c) Example of stiffness map (elastogram) representing spatial values of G_1. 14

Figure 2-2: Real part of SLDV acquired amplitude Frequency Response Function (FRF) curve fitting example from the large diameter Ecoflex specimen at an excitation frequency of 150 Hz. 17

Figure 2-3: Imaginary part of SLDV acquired amplitude Frequency Response Function (FRF) curve fitting example from the large diameter Ecoflex specimen at an excitation frequency of 150 Hz. 18

Figure 3-1: Construction of multi-layer Ecoflex phantom used in Phase 1 pressure loading study. (a) Large circular bar used to form outer layer. (b) Outer layer final solidification. (c) Small circular bar used to form inner layer 21

Figure 3-2: Completed multi-layer phantom is shown placed in water for visual air bubble leak pressure testing before experiments. 22

Figure 3-3: Cast used to mold tensile specimen. (a) Full cast ready for pouring mold with specimen also shown. (b) Two identical cast sections showing specimen shape machined from 15.24 cm long x 3.49 cm diameter aluminum bar and bottom cast holder; also specimen shown in one of the cast sections after solidification. 23

Figure 3-4: Cylindrical 5.5" and 2.5" specimens used for optical validation study. Plastisol is shown in image. Ecoflex was used in identical cylinders. The circular disks for the solidification process are shown removed below each corresponding cylinder. 24

Figure 4-1: Ecoflex multi-layer phantom schematic with outer soft layer, inner hard layer, and inner pore for variable pressure loading source. 28

Figure 4-2: (a) Air filled pore in multilayer phantom for variable pressure loading. (b) Liquid filled pore 29

Figure 4-3: Multilayer phantom mounted in MRI insertion platform and connected to piezoelectric actuator. Plastic hose inserts into phantom for pore pressure control. 29

Figure 4-4: Piezoelectric stack used to vibrate phantoms in MRE experiments. 29

Figure 4-5: Translation actuation is induced into phantom by mounting it to a rod connected to a grounded oscillating piezo. The phantom slides freely on the MRI insertion platform. 30

LIST OF FIGURES (continued)

FIGURE PAGE

Figure 4-6: MRE workflow to calculate average shear modus for outer and inner layer of multilayer phantom with pore air pressure = 0. (a) Magnitude image used to segment each stiffness region used in processing date. (b) Example of wave propagation through phantom where the inner layer experiences longer wavelengths than the outer stiffer layer. (c) Shear modulus stiffness map with the outer layer of a different stiffness than the inner. 30

Figure 4-7: Pressure gauge used to monitor regulated pressuring loading into phantoms. 30

Figure 4-8: Phantom layers in compression from volume change due to internal pressure loading of air filled pore (a) Air pore at max pressure = 150 mm/Hg. (b) Air pore at atmospheric pressure = 0 mm/Hg. (c) "Image b" subtracted by "Image a" to visualize compression strain from the change in pore pressure. 31

Figure 4-9: Data legend for plots in Figure 4-10, Figure 4-11, and Figure 5-12. 32

Figure 4-10: Average MRE shear modulus for each layer from the multilayer phantom over all 4 cycles during air and liquid pressure loading. 32

Figure 4-11: MRE displacement amplitude (perpendicular to the phantom axial direction) of inner and outer layers during air and liquid pressure loading in multilayer phantom. 34

Figure 4-12: Hysteresis observed in the outer soft layer during 4 cycle of liquid pressure loading. 35

Figure 5-1: Ecoflex multi-layer phantom schematic with outer soft layer, inner hard layer, and inner pore for variable pressure loading source. 38

Figure 5-2: (a) Big and small wires used for interconnected porosity network in phantom regions. (b) Wire network placed in rigid plastic cylinder. (c) Ecoflex solidification around wire network in cylinder. (d) Back side of cylinder with rigid plastic disk glued in place. (e) Additional plastic disk with barb fitting is glued onto other end of cylinder once wires and perforated copper tube are extracted from the solidified Ecoflex. 39

Figure 5-3: MRI magnitude images of one Ecoflex interconnected porosity phantom quadrant. Top row are axial images and bottom row are coronal slices. 40

LIST OF FIGURES (continued)

FIGURE PAGE

Figure 5-4: (a) Isometric surface produced from high-resolution MRI magnitude images of one interconnected porosity phantom quadrant. (b) Front view of isometric. (c) Axial images of the interconnected porosity phantom. The magnitude image, wave *x*-motion, *y*-motion, and *z*-motion are displayed from left to right, respectively. The areas within the yellow dotted lines drawn on the magnitude images represent the big pore region and the small pore region indicated with a yellow "a" and "b", respectively. (e) Description of rotational motion used for phantom mechanical excitation (phantom in yellow) 41

Figure 6-1: Ecoflex specimen used for simultaneous tensile testing and MRE. The red dotted line rectangles depict the approximate locations of the imaged regions 45

Figure 6-2: Photos of Tensile-MRE probe and components. (a) Full view of probe with 213.4 cm length and 3.8 cm outside diameter. (b) Load cell attached to elongation slide. (c) View looking down the center of the probe showing the actuator locking rod. (d) Two piezoelectrics placed in parallel attached to the beveled locking head and ram. (e) Actuator grip mechanism. 49

Figure 6-3: Schematic of Tensile-MRE probe internal components. All components sit inside a transparent polycarbonate tube. (a) Load cell mounted on adjustable elongation slide. (b) Tension string. (c) Locking head. (d) Piezoelectric actuators. (e) Actuator sleeve. (f) Heat shrink tubing. (g) Air syringes. (h) Mounting screw. (i) Tension rod between air syringe extension and grip collar compression. (j) Pulling ring. (k) Ecoflex 0010 specimen. (l) Grip collars. (o) Grips. (m) Probe end cap. 49

Figure 6-4: Actuator grip mechanism. (a) Actuator sleeve removed to show AGM internal components. Two air syringes transfer a closing tension to the grip collars through four garolite rods. (b) Front view of grip sizes with small, medium, and big on top, middle, and bottom, respectively. (c) Side view of grip sizes in same order as image b. (d) Depiction of grip collars and beveled grips used to transfer longitudinal expansion motion of syringes to radial clamping motion around the specimen. 50

Figure 6-5: ROI-averaged values of MRE-derived (a) 3D shear storage modulus and (b) displacement using f_e = 2.0 kHz and 140 % strain. The grip air pressure was increased in increments of 0.7 bar (corresponding to approximately 10 psi). 51

LIST OF FIGURES (continued)

FIGURE PAGE

Figure 6-6: Axial images of a central slice for specimen at 0 and 140 % strain and using f_e = 2.0 kHz. The magnitude image, wave *x*-motion, *y*-motion, *z*-motion, and *G* stiffness map (shear storage modulus) are displayed from left to right, respectively. The areas within the black dotted lines drawn on the magnitude images represent the masked ROIs used for all image post processing and averaging. Separate ROI masks were constructed for each strain increment to match the changing specimen diameter in response to elongation. Wave motion represents displacement perpendicular to image plane. 52

Figure 6-7: MRE-derived complex shear modulus in the strain range 0 to 140 % for f_e = 1.5, 2.0, and 2.5 kHz. (a) *G* storage modulus vs. strain. (b) *G* loss modulus vs. strain. (c) *G** storage modulus vs. strain. (d) *G** loss modulus vs. strain. *Of note, the complex shear modulus at 140 % strain with f_e = 1.5 kHz is considered an outlier and not displayed in the figure..... 52

Figure 6-8: Comparison between 2D and 3D inversion shear storage moduli at f_e = 2.0 kHz. (a) *G*, *G**, g_x, g_y, g_z, vs. strain. (b) *G** directional components vs. strain. 53

Figure 6-9: (a) Comparison between tensile stress and G_n. (b) Experimental tensile stress, Fung hyperelastic model tensile stress, and normalized storage shear modulus at f_e = 0 kHz plotted with strain. T: Experimental tensile stress from. T_{Fung}: Fung model tensile stress from (2.25) with G_{inft} = 7.01 kPa and b = 0.17 with R^2 = 98.9 %. G_n: G_n (f_e = 0 kHz). 54

Figure 7-1: (A) Cylindrical specimens used in experiments (Ecoflex and Plastisol to the left and right, respectively). Numbers indicate softener concentration percentage. (B) Actuation system with piezoelectric connected to actuation disk pressed onto the large diameter Plastisol specimen. 64

Figure 7-2: Schematic representing the experimental platform used for synchronous acquisition of SLDV and MRE of a large diameter cylindrical specimen. 65

Figure 7-3: (A) First-surface mirror used in experiments. (B) Large cylinder specimen in center of magnet. (C) Polar grid of SLDV data points seen through SLDV user interface overlaid onto specimen front surface..... 66

LIST OF FIGURES (continued)

FIGURE PAGE

Figure 7-4: Comparison between surface and internal displacement fields for the large Ecoflex specimen with increasing frequency acquired by SLDV and MRE, respectively (perpendicular to specimen radial plane). Data was collected synchronously between both imaging modalities for each individual excitation frequency. (A) 60, (B) 100, (C) 150 Hz for MRE. MRE wave motion images are from the axial slice of 4 mm thickness closest to specimen front surface. (D) 60, (E) 100, (F) 150 Hz for SLDV. SLDV wave images are acquired from the specimen front surface. (G) 60 Hz, (H) 100 Hz, (I) 150 Hz of a 1D displacement profile using a horizontal line across the entire specimen diameter passing though its center Images in top two rows are extruded to isosurface plots. 69

Figure 7-5: Comparison between surface and internal displacement fields for the small Ecoflex specimens with increasing specimen stiffness at 250 Hz acquired by SLDV and MRE, respectively (perpendicular to specimen radial plane). (A) 40, (B) 25, (C) 10 % softener concentration for MRE. (D) 40, (E) 25, (F) 10 % softener concentration for SLDV. (G) 40, (H) 25, and (I) 10 % softener concentration of a 1D displacement profile using a horizontal line across each specimen diameter passing though its center. Images across the top of the figure are extruded to isosurface plots.....70

Figure 7-6: MRE and OE values for complex shear modulus for increasing frequency and specimen stiffness with Plastisol and Ecoflex. The p value represents a student t-test between MRE and OE moduli for each varying frequency and stiffness scenario with $p > 0.05$ meaning the values in the comparison are not significantly. Error bars represent standard deviation with 3 samples per data point. Real and imaginary parts of the complex shear modulus are at the right and left sections of the individual bar graphs, respectively.. 72

Figure 7-7: Correlation between MRE and OE complex shear moduli related by coupled scan. Data points include all 36 sets of scans obtained in study for variations in frequency, stiffness, and material.....76

Figure 7-8: SLDV system set up for synchronous MRE and SLDV experiments.....76

LIST OF ABBREVIATIONS

AGM	Actuator Grip Mechanism
CT	Computed Tomography
DV	Divergence
FOV	Field of View
MEG	Motion Encoding Gradient
MR	Magnetic Resonance
MRE	Magnetic Resonance Elastography
MRI	Magnetic Resonance Imaging
NMR	Nuclear Magnetic Resonance
OE	Optical Elastography
RF	Radio Frequency
ROI	Region of Interest
SLDV	Scanning Laser Doppler Vibrometry
SLIM	SampLe Interval Modulation
TE	Time of Echo
TR	Time of Repetition

SUMMARY

The contents of this dissertation include investigations in Magnetic Resonance Elastography (MRE) using a preclinical 9.4 Tesla small animal Magnetic Resonance Imaging (MRI) system along with synthetic materials that mimic the mechanical properties of soft biological tissue. MRE is used for studying the mechanical behavior of soft tissue particularly applicable to medical applications. Motion induced by a mechanical driver is measured with MRI to acquire internal displacement fields over time and space within a material media. Complex shear modulus of the media is calculated from the response of mechanical wave transmission through the material. Changes in soft tissue stiffness are associated with disease progression and this is why assessing tissue mechanical properties with MRE has powerful diagnostic potential. The experiments performed in this dissertation used elastic phantoms and specimens to observe the influence of pre-stress on MRE derived mechanical properties while additional mechanical measurements from other related material testing methods were synchronously collected alongside MRI scanning.

An organ simulating phantom was used to explore changes in MRE stiffness in response to gas and liquid cyclic pressure loading. MRE stiffness increased with pressure and hysteresis was observed in cyclic pressure loading. The results suggest MRE is applicable to pressure related disease assessment. In addition, an interconnected porosity pressure phantom was constructed for future porous media investigations.

A custom system was also built to demonstrate concurrent tensile testing during MRE for investigating homogeneous soft material media undergoing pre-tension. Stiffness increased with uniaxial tensile stress and strain. The tension and stiffness relationship explored can be related to the stress analysis of voluntary muscle. The results also offer prospective experimental strategies for community wide standards on MRE calibration methods.

Lastly, a novel platform was developed for synchronous acquisition of Scanning Laser Doppler Vibrometry (SLDV) and MRE for examining surface wave dynamics related to internal media wave propagation in soft material experiencing sinusoidal mechanical excitation. The results indicate that displacement measurements of media on the surface are similar in nature to internal displacement measured from MRE. It is concluded that optical and MRI based elastography yield similar values of complex shear modulus.

CHAPTER 1

INTRODUCTION

1.1 Motivation

The primary reasoning for conducting the projects in this dissertation was to develop novel experimental techniques for investigating MRE's ability to measure changes in soft material stiffness related to pre-stress and also to compare MRE results to other material testing methods. These supplementary testing methods are related to MRE for directly quantifying mechanical properties (stiffness) of synthetic tissue-mimicking material in search of ways to systematically calibrate MRE measurements. The work contains novel MRI platforms that use synchronous data acquisitions including SLDV and uniaxial tensile testing. Calibration standards for MRE scanning in the research and clinical communities, currently do not exist. Ultimately, to improve future patient MRE diagnostic quality, standard practices need to be developed and implemented.

Another subproject regarding pre-stress includes investigating the ability of MRE to measure internal tissue pressure. A soft material phantom of varying compound stiffness was built to measure stiffness changes in response to internal gas and liquid pressure loading. This is relevant for noninvasively diagnosing hydrocephalus, hypertension, tumors, and edema using MRE. The relation of physiological pressure changes in organs and MRE derived stiffness are not well understood. The pressure experiments provide insight on how pressure loading relates to MRE derived stiffness changes of soft tissue mimicking material.

1.2 Synthetic Materials for Mimicking Soft Biological Tissue

The experiments in this dissertation use Ecoflex (00-01, SMOOTH-ON, INC., USA) and Plastisol (Soft Plastic, Alumilite Corporation, USA), which can be imaged with ^{1}H MRI and have similar

viscoelastic mechanical properties as soft biological tissue (Pickup & Thomson 2010; Leclerc et al. 2012). Akin to soft tissue, Ecoflex MRE derived stiffness increases with excitation frequency (Liu et al. 2014; Yasar et al. 2013; Klatt, Friedrich, et al. 2010). Both materials are silicon based. Although elastography experiments ultimately need to be performed on biological tissue and with in vivo studies, using these materials for phantoms and specimens studies is beneficial. Both Ecoflex and Plastisol can be molded into complex geometries for simulating organs. The material stiffness can also be altered to control mechanical properties.

1.3 A Brief Historical-Based Overview of MRI

The following section is intended to be a brief technical explanation of MRI based on significant historical discoveries and publications, which allowed MRI to evolve from theories to a practical clinical tool. MRI is a very complex concept as it uses components from chemistry, physics, engineering, and medicine. Many avenues may still unfold for its use in medicine and other scientific research as innovation continues in hardware development and computer processing.

Previous to any reputable experimental proof of the atom and its components, many physicists agreed that all matter was made up of some type of fundamental element. Several theories existed but not until quantitative measurement of electricity was available in the mid to late 1800's could theory be backed with experimental evidence that the atom existed and is made up of multiple particles. The first significant component related to MRI is the idea that angular velocity rotation and alignment of protons are related to the strength and direction, respectively of its surrounding magnetic field. Joseph Larmor was attributed for this theory and thus the idea was named the Larmor frequency in (1.1) where ω is the Larmor frequency, γ is the gyromagnetic ratio (267.513 MHz $T^{-1}$for ^{1}H proton that is the most common particle used to produce information in MRI), and B_0 is the magnetic field strength (Larmor 1896).

$$\omega = -\gamma B_0 \tag{1.1}$$

MRI systems use a very strong main magnetic field constructed of superconducting magnetic solenoids to align and induce proton rotation in biological tissue within the scanner. Biological tissue is largely comprised of water built upon ^{1}H protons and is why it is very responsive within strong magnetic fields. The angle of a proton rotating axis is forced towards the direction of the main magnetic field. This was first investigated by Isidor Isaac Rabi who introduced new theories of proton precession axis direction in expansion of the Stern–Gerlach experiment. Protons spin approximately 54.7 degrees off the axis of the main magnetic field direction (Rabi et al. 1934; Gerlach & Stern 1922).

Another significant discovery related to MRI occurred when Felix Bloch in 1946 published an article describing how protons rotating in a static magnetic field pulse (tilt of rotating axis) if subjected to a perpendicular rotating magnetic field (Bloch 1946). This was the beginning of Nuclear Magnetic Resonance (NMR) spectroscopy where specimen bulk material contents can be analyzed. However, no spatial information could be accessed (no image). Protons pulse when the rotating magnetic field frequency matches the proton Larmor frequency. Radio Frequency (RF) coils are designed to fit inside main field magnets to induce rotating magnetic fields within a Region of Interest (ROI).

Perhaps the most significant contribution to MRI is when Paul C. Lauterbur in 1973 published a paper on forming images with NMR (Laubertur 1973). Spatial information is obtained by using gradient coils to produce linear variations of the magnetic field over a region being imaged. The strategic application of the magnetic field gradients results in protons having different spatially dependent angular frequencies that are used to form the spatial characteristics of the Magnetic Resonance (MR) image.

All of these components of MRI are used together in one system containing a main magnet, gradient coils, and RF coils. The magnetic fields from these components are scripted together in time dependent signals in a pulse sequence that manipulates protons to produce cross sectional images of the insides of a human or specimen. The greatest benefit of MRI is its ability to noninvasively and internally image using non-ionizing radiation that does not pose a significant risk to the patient. However, MRI does

have some drawbacks. Costs of hardware and image data acquisition time are the bigger limitations but as magnet technology improves and pulse sequencing becomes more efficient, these problems will likely diminish.

1.4 Magnetic Resonance Elastography

MRE is a noninvasive imaging method for obtaining mechanical properties of soft tissue. External vibrations are introduced into a ROI. The state of vibration is measured with phase contrast MRI from which ROI tissue stiffness is calculated. MRE is currently being investigated for stiffness changes related to fibrosis and neurodegeneration diseases (Ehman et al. 2012). Several other preliminary studies have assessed MRE potential in other soft tissue organs such as the heart, skeletal muscle, and lungs (Tse et al. 2009).

In 1991, Lewa theoretically proposed that variations in MRI signal phase are manipulated by sinusoidal mechanical wave transmissions in elastic soft material (Lewa 1991). The first paper introducing MRE was published by Muthupillai in 1995 where the idea of imposing Motion Encoding Gradient (MEG) waveforms over a MRI pulse sequences was used to measure mechanical vibration for yielding material stiffness (Muthupillai et al. 1995). The type and position of the external vibration source should be chosen according to the target ROI. For example, a passive drum actuator placed over the abdomen can be used for liver MRE and a hinged rocker connected to a piezoelectric actuation device, in which the head is positioned, can be used for brain MRE. Particle displacement measurement is achieved by synchronizing the vibration source to MEGs. Protons accumulate phase within the vibrating particles as the MEG change the proton angular frequency over time and space. The particle displacement is equivalent to phase resolved images acquired from the MRI data. Offsetting the vibration phase from the MEG waveform with multiple time steps allows the acquisition of a full wave propagation cycle through a ROI. Tissue shear modulus (stiffness) is obtained by calculating the shear wave speed of the

propagating shear wave. The stiffness can be displayed as a stiffness map or averaged over a ROI to diagnose a particular stiffness change relative to disease.

MRE is among several other elastography methods that can obtain human soft tissue stiffness. Other examples are ultrasound elastography, SLDV based optical elastography, and optical coherence topographic elastography. MRE has an advantage over the other methods since it can obtain stiffness values of the brain. Ultrasound and optical images can not yet penetrate through the skull. Similar in all elastography methods, yielding stiffness is dependent on mechanical excitation frequency and tissue pre-stress condition. A handful of assumptions are also made about the tissue ROI when calculating stiffness in MRE. The inversion techniques in this dissertation assume the target material is isotropic, locally-homogeneous, and incompressible with density equal to water (1,000 Kg/m^3) and Poisson's ratio = 0.4999. These parameters are used in the majority of MRE studies.

1.5 MRE Data Collection

This section is intended to be practical instruction for collecting experimental MRE data and handling custom MRE hardware. The diagnostic portion stems mainly from experiences learned from conducting phantom experiments reported in this dissertation on the 9.4 T preclinical MRI system. However, the lessons learned can be applied to animal and human MRE systems, as well.

Most importantly, safety is the biggest concern especially when new and custom hardware is being used in high magnetic fields. The new system may be overlooked for MRI compatibility in the material it is built from, electrical hazards, and mechanical function. It is best to have other MRI professionals look over the new hardware design before operating the system in the magnet environment. There are many materials available on the market with different material content. Some of which may appear to be plastic but should always be checked in a magnetic field for magnetic attraction prior to putting the material next to the MRI magnet. Also since MRE involves actuation, the materials may act

different when in motion in a magnetic field than when static. The pretest should take material movement into account. When systems use piezoelectric actuators, strong electrical power is sometimes used to control the actuator. Precaution must be taken to avoid electrical shock to research personnel, subject, or to the MRI system itself. Also, when designing custom piezoelectric motion devices, use caution to make sure no unwanted bending, torque, tension, compression, or bending occurs while attaching specimens to an actuation device, loading an apparatus into magnet, transporting an apparatus, repositioning an apparatus in the magnet, or during actual mechanical actuation of specimens while performing MRE scans.

MRE experiments should be started with positioning the specimen in the magnet center using a quick scan of multiple slices of axial, sagittal, and coronal views (the so-called "scout" MRI scan). The next step is to use short MRE scans with one phase offset to optimize scan parameters for finding applicable wave propagation in the specimen. Parameters such as excitation frequency, piezo amplitude, mechanical actuation pre-cycles, MEG strength, MEG cycles, repetition time, echo time, FOV, matrix size, slice thickness, number of slices, and scan averages can be adjusted to fine tune the characteristics of the wave propagation and the quality of the MR signal. Many other MRI parameters can be adjusted to enhance the MR signal but the focus of this section is to optimize the acquisition of wave propagation in MRE. The following steps are practical methods and troubleshooting instructions for acquiring good MR signal and to adjust MRE pulse sequence parameters to obtain suitable wave motion for MRE experimentation:

<u>Initial parameters to begin MRE pretests with:</u>

- Start with Minimum TR and TE.
- Only increase TR if MR signal is weak.

- Choose starting # of MEGs based on what MRE publications have used containing similar specimens to the specimen currently being imaged.
- Start with lower MEG gradient strength.
- Start with close to full power in piezo amplitude (do not overpower piezoelectrics because they can burn out easily, try to run a couple amplifier setting below max achievable electrical power to avoid this potential damage lengthy scans).

Action when getting noisy MR signal:

- Check that the specimen is grounded to the center of the Magnet.
- Check if the BNC wires are completely connected to the RF coil.
- VISUAL CHECK to make sure data was collected after each scan and save the data to another storage drive after each scan instead of at the end of the session.

Check-list for the case that no waves are present with a good MR signal:

- Is piezo turning on:
- Wire possibly not connected properly to piezo.
- Piezo may be broken.
- Is the actuator or its components loose in any places.
- Are all settings on MRE cart correct.
- Connections in cart could be unconnected or the junction box could be broken.
- Is the MRE structure ground properly to the magnet and not slipping during actuation.

Check in the case of unconventional wave patterns:

- Extreme phase wraps: lower piezo amplitude.
- Weak waves: increase cycle number and/ or amplitude of MEGs.
- Less than one wavelength inside ROI: increase excitation frequency.
- Waves present but blurry: increase spatial resolution.
- Waves attenuate too quickly over distance from actuation source: lower excitation frequency.
- MR signal becomes lower as number of slices is increased: lower number of MEGs and/ or increase TR.

After each final MRE scan is finished it is recommended to:

- Visually check to make sure data was collected after each scan.
- Run all phase offset images in a video within Matlab or available processing software to be sure that the wave is propagating.

CHAPTER 2

THEORY AND DATA PROCESSING

The theory and data processing of all material mechanical properties used in this thesis are described here. TABLE I includes all mechanical property variables by name and derivation equation. Also, the MRE image data analysis workflow used in all studies is explained. Most all data from this dissertation is processed in Matlab (MathWorks, USA).

TABLE I
CALCULATED MECHANICAL PROPERTIES LIST

Variable Name (Pascal)	**Variable**	**Equation**
Shear Modulus (complex, with curl)	G_1	2.8
Longitudinal Modulus (complex)	L	2.12
Shear Modulus (complex)	G	2.12
X-direction Shear Modulus	g_x	2.15
Y-direction Shear Modulus	g_y	2.15
Z-direction Shear Modulus	g_z	2.15
Amplitude Weighted Shear Modulus (complex)	G^*	2.16
Tensile Stress	T	2.17
Longitudinal Strain (engineering strain)	ϵ	2.18
Fung Hyperelastic model Tensile Stress	T_{Fung}	2.25
Optical Elastography Shear Modulus (complex)	G_{su}	2.30

2.1 Wave Equation and Inversion Methods

All MRE moduli are calculated from inversion methods that are based on the Navier wave equation,

$$\rho \frac{\partial^2}{\partial t^2}\mathbf{u} = (\lambda + \mu)\nabla(\nabla \cdot \mathbf{u}) + \mu\Delta\mathbf{u} \tag{2.1}$$

where $\boldsymbol{u}$ is the 3D displacement vector of the propagating wave, f is frequency ∇ is the Divergence (DV) operator, Δ is the Laplace operator as defined in (2.2), λ is the first Lame parameter, and μ is the second

Lame parameter. (2.1) represents the equation of motion of a continuum under the assumptions of isotropy, linear elasticity, and local homogeneity.

$$\Delta f = \frac{\partial^2 f}{\partial x^2} + \frac{\partial^2 f}{\partial y^2} + \frac{\partial^2 f}{\partial z^2} \tag{2.2}$$

The Lame parameters λ and μ are also known as the longitudinal modulus and shear modulus, respectively. The shear characterizes the shear wave propagation in a material and the longitudinal modulus together with the shear modulus characterize compression wave propagation in a material. Young's modulus, E can be derived from λ and μ by (2.3).

$$E = \frac{\mu(3\lambda+2\mu)}{\lambda+\mu} \tag{2.3}$$

(2.1) is next converted into the frequency domain using the Fourier Transform (2.4).

$$F(\omega) = \int_{-\infty}^{\infty} f(t) e^{-i\omega t}\, dt \tag{2.4}$$

With its properties,

$$\{\frac{df(t)}{dt}\ [i\omega F(\omega)] \text{ and } \frac{d^2 f(t)}{dt^2}\ [-\omega^2 F(\omega)]\}$$

Converting (2.1) to frequency domain using (2.4) yields (2.5).

$$-\rho\omega^2 \mathbf{U}(\omega) = (L(\omega) + G(\omega))\nabla\big(\nabla \cdot \mathbf{U}(\omega)\big) + G(\omega)\Delta\mathbf{U}(\omega) \tag{2.5}$$

Where ω is the angular frequency of the wave motion, L is the complex longitudinal modulus, G is the complex shear modulus, The complex wave image **U** corresponds to the Fourier Transform of the 3D displacement **u**. Each complex modulus has a real and imaginary part corresponding to the storage modulus and loss (damping) modulus, respectively, that relate to the materials ability to absorb and loose energy during wave propagation.

The shear modulus can be calculated by two methods. One method uses a curl operator to disregard *L* by filtering the compression wave (Sinkus *et al* 2007). The other method does not filter the compression wave and yields *L* in addition to *G*. Shear modulus will be defined as G_1 (with curl) and *G* (without curl). The curl operator is defined in (2.6)

$$\mathbf{Q} = \nabla \times \mathbf{U} \tag{2.6}$$

Applying (2.6) to (2.5) yields,

$$-\rho\omega^2\mathbf{Q}(\omega) = G_1(\omega)\Delta\mathbf{Q}(\omega) \tag{2.7}$$

Using the least squares solution yields G_1 in (2.8) where $^{-1}$ is the inverse of a tensor and ^{T} is the transpose.

$$G_1 = -\rho\omega^2[(\Delta\mathbf{Q})^T\Delta\mathbf{Q}]^{-1}(\Delta\mathbf{Q})^T\mathbf{Q} \tag{2.8}$$

Not using the curl operator to find *L* and *G* is done by first rearranging (2.5) to (2.9) (Oliphant *et al* 2001).

$$-\rho\omega^2\mathbf{U}(\omega) = L(\omega)\nabla\big(\nabla\cdot\mathbf{U}(\omega)\big) + G(\omega)\big[\Delta\mathbf{U}(\omega) + \nabla\big(\nabla\cdot\mathbf{U}(\omega)\big)\big] \tag{2.9}$$

And using a compact form with tensor $\overline{\mathbf{A}}$,

$$-\rho\omega^2\mathbf{U}(\omega) = \overline{\mathbf{A}}\begin{bmatrix}G\\L\end{bmatrix} \tag{2.10}$$

where U_1, U_2, U_3 are the orthogonal components of $\boldsymbol{U}$ and x_1, x_2, x_3 are the orthogonal spatial directions.

$$\overline{\mathbf{A}} = \begin{bmatrix}\Delta\mathrm{U}_1 + \frac{\partial}{\partial\mathrm{x}_1}(\nabla\cdot\mathbf{U}) & \frac{\partial}{\partial\mathrm{x}_1}(\nabla\cdot\mathbf{U})\\ \Delta\mathrm{U}_2 + \frac{\partial}{\partial\mathrm{x}_2}(\nabla\cdot\mathbf{U}) & \frac{\partial}{\partial\mathrm{x}_2}(\nabla\cdot\mathbf{U})\\ \Delta\mathrm{U}_3 + \frac{\partial}{\partial\mathrm{x}_3}(\nabla\cdot\mathbf{U}) & \frac{\partial}{\partial\mathrm{x}_3}(\nabla\cdot\mathbf{U})\end{bmatrix} \tag{2.11}$$

The least squares solution of (2.10) then yields (2.12) for *L* and *G*.

$$\begin{bmatrix} G \\ L \end{bmatrix} = -\rho\omega^2[\overline{\mathbf{A}}^T\overline{\mathbf{A}}]^{-1}\overline{\mathbf{A}}^T\mathbf{U} \tag{2.12}$$

Of note, the derivate operators in (2.11) correspond to the 3D Del and Laplace operators. When only one image slice is acquired, the material is assumed to be incompressible (2.13).

$$\nabla \cdot \mathbf{U} = 0 \tag{2.13}$$

A simplification of (2.5) after using (2.13) gives (2.14) where *G* becomes the scalar 2D inverted shear modulus.

$$-\rho\omega^2\mathbf{U} = G\Delta\mathbf{U} \tag{2.14}$$

Then (2.15) yields g_i where $i = x, y, z$ depending on the wave displacement direction.

$$g_i = \frac{-\rho\omega^2 \mathrm{U_i}}{\Delta \mathrm{U_i}} \tag{2.15}$$

Shear characteristics can also be presented in the form of G^*, which is defined as the sum of g_x, g_y, and g_z weighted by the amplitudes of the displacement projections by,

$$G^* = R_x g_x + R_y g_y + R_z g_z, \text{ and } R_i = \frac{|U_i|}{|U_x|+|U_y|+|U_z|} \tag{2.16}$$

$R_i g_i$ is the directional component of G^* (Liu et al. 2016; Kolipaka et al. 2012).

A shear storage modulus G_n, which is normalized to the result of the undeformed state (used in tensile testing experiments) is defined as

$$G_n\,(f, \varepsilon) = G'\,(f, \varepsilon) - G'\,(f, \varepsilon = 0), \tag{2.16.a}$$

where G' represents the real part of G, in order to examine changes in stiffness related to pre-tension deformation.

2.2 MRE Data Processing

All MRE data collected in the studies of Chapters 4, 6, and 7 are processed using a Master Script. Material mechanical properties in TABLE I are calculated for all studies. However, only specific mechanical properties were reported in the results sections of each study depending on their significance to the investigation. The generalized data processing workflow of the Master Script is described in the following.

The first step in the workflow is to mask out the ROI in the image slices. Depending on what is more clear for visually selecting the ROI, either the unmasked magnitude or wave motion images are used for masking. A rule of thumb is to always select a few pixels away from the specimen edges. An example of this is shown for the large cylindrical Ecoflex sample used in Chapter 7 with excitation frequency f = 150 Hz (Figure 2-1(a)).

Data is next run through a phase unwrapping algorithm. Protons sometimes accumulate too much phase from the interaction between mechanical excitation and MEGs. Phase wrap distortions show up in wave motion images and affect the accuracy of inversion methods to calculate shear modulus. Data processed through the unwrapping algorithm not needing phase wrap correction remains unaffected.

At each offset, phase-difference images were calculated to filter contributions of static field inhomogeneities. The complex wave images were taken from the 1st harmonic after Fourier transformation of temporally-resolved phase-difference images where the wave motion becomes visual (Figure 2-1(b)). Data was then plugged into (2.12) to calculate the complex moduli of the first and second Lame-parameter, L and G in addition to shear modulus, G_1 using the curl operator in (2.8) (Figure 2-1(c)). The x, y, and z-motion were run through (2.15) separately yielding 2D shear moduli, g_x, g_y, g_z, respectively. Amplitude Weighted Shear Modulus, G^* is then calculated using (2.16). Prior to both, 2D and 3D inversion the complex wave images were filtered using a spatial Butterworth band pass with a lower and upper filter limit of 6 pixels and half of the Field of View (FOV), respectively. In order to

prevent edge effects, all moduli were spatially averaged over innermost slices, while excluding outliers > 200 kPa.

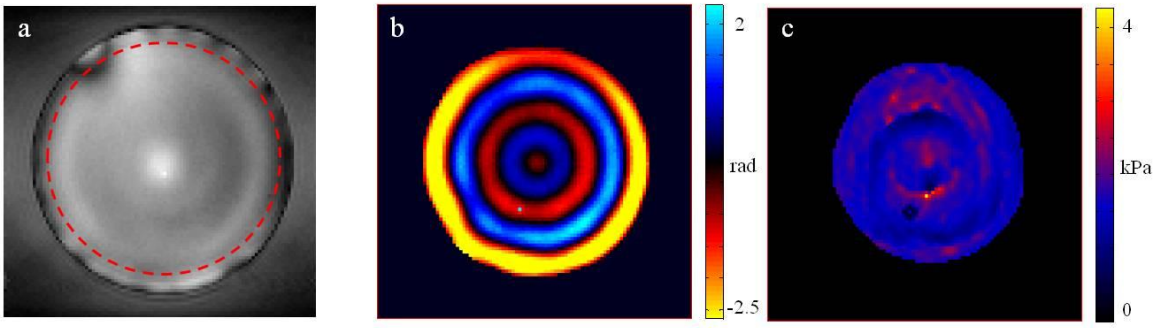

Figure 2-1: (a). Magnitude image of axial slice with red dotted line representing masked out ROI. (b). Snapshot of wave propagation with displacement perpendicular to imagine plane. (c) Example of stiffness map (elastogram) representing spatial values of G_1.

2.3 Tensile Testing and Hyperelastic Theory

The following formulas were used to calculate all variables for the tensile testing study in Chapter 6. Tensile stress, *T*, is calculated using (2.17). The specimen used was assumed to be homogeneous, elastic, isotropic, and incompressible. Strain, ϵ is given by

$$\epsilon = \frac{l - l_0}{l_0}, \tag{2.17}$$

where l_0 and l correspond to specimen lengths between the ends of the pulling rings before and after imposing uniaxial deformation, respectively (Figure 6-1). Tensile stress *T* is defined as

$$T(\epsilon) = \frac{F(\epsilon)}{A_0} \tag{2.18}$$

with tensile force *F* measured using a load cell and cross sectional area A_0 of the unstressed specimen. Stretch ratio λ is defined by

$$\lambda = \epsilon + 1. \tag{2.19}$$

Experimental stress and strain data define the mechanical behavior of a material and can be fitted to the stress-strain relation of a specific model. In the present work we chose the Fung hyperelastic strain energy model to describe the measured stress response to large uniaxial tensile deformation (Rashid et al. 2014; Fung et al. 1979; Fung YC 1967). Models such as the Mooney Rivlin or Neo-Hookean use multiple invariants whereas the Fung theory uses only the first invariant, thus the Fung model was selected for simplicity (Miller 2001). The Fung strain-energy density function W using the principle strain invariant I_1,

$$W = W(I_1) = \frac{G_{inft}}{2b}\left(e^{b(I_1-3)} - 1\right), \tag{2.20}$$

$$I_1 = \lambda_1^2 + \lambda_2^2 + \lambda_3^2, \tag{2.21}$$

and infinitesimal shear modulus G_{inft}, which corresponds to the shear storage modulus without tensile deformation, and stiffening parameter b**.** The invariant within the model characterizes a hyperelastic incompressible material. Fung models are often used to represent soft biological tissue in tension (Rashid et al. 2014). Assuming incompressibility and symmetry (the direction of tension being aligned with the stress and strain) allows the principle stretch ratios to be related as $\lambda_1\lambda_2\lambda_3 = 1$. Homogeneous deformation is assumed during tension, so stretch ratios are,

$$\lambda_1 = \lambda \ and \ \lambda_2 = \lambda_3 = \frac{1}{\sqrt{\lambda}} \tag{2.22}$$

where $\lambda \geq 1$ is the stretch ratio in direction of tensile force. With these assumptions I_1 becomes,

$$I_1 = \lambda^2 + 2\lambda^{-1} \tag{2.23}$$

Stress and strain energy functions are related by,

$$\text{Tenisle Stress} = \frac{\partial W}{\partial \epsilon}. \tag{2.24}$$

Plugging (2.20) into (2.24) with the invariants yields the tensile stress T_{Fung} of the Fung model along the direction of tensile force,

$$T_{Fung} = G_{inft} e^{b\left(\lambda^2+2\lambda^{-1}-3\right)}\left(\lambda-\lambda^{-2}\right). \quad (2.25)$$

The Fung model tensile stress, T_{Fung}, (2.25) was fitted to the experimental T for determining G_{inft} and b.

2.4 SLDV and Line Profile Curve Fitting

In Chapter 7, 1D surface wave line profiles from the cylindrical specimen front surfaces were collected. Each of the 8 lines from the polar array were individually curve fit to the objective function, FRF_{obj} (2.26) using MATLABs nonlinear curve fitting algorithm. The objection function includes variable of r = radial position along the specimen front surface, a = the specimen front surface radius, X_1 = amplitude correction, X_2 = phase correction, X_3 = center offset correction, and X_4 = compression wave correction, X_5 = gravity correction, X_6 = surface wrap correction, $j = \sqrt{-1}$, k = surface wave number, ρ = density, ω = angular velocity, G_{su} = optical elastography complex shear modulus, and ν = Poisson's ratio. The search algorithm for the minimum used the 'Levenberg-Marquardt' algorithm. This minimized the error function in (2.27) (see equation 9 in (Kearney et al. 2015) for further details on (2.27), (2.28) and derivations for Bessel functions k_2 and I_o). After k is estimated from curve fitting, the surface wave number can then be related to the shear wave number by finding the roots of (2.28). Equations (2.29) and (2.30) yield G_{su} where the mean value is calculated from all 8 lines of the SLDV polar grid.

$$FRF_{obj} = X_1 e^{jX_2}\frac{I_0(jK(r-X_3))}{I_0(jaK)} + X_4 + X_5 r + X_6 r^2 \quad (2.26)$$

$$Error = min\sum_{i=1}^{n} FRF_{obj}(X, xdata_i) - ydata_i)^2 \quad (2.27)$$

$$p^3 - 8p^2 + \left(24 - 16\left(\frac{1-2\nu}{2(1-\nu)}\right)\right)p - 16\left(1 - \left(\frac{1-2\nu}{2(1-\nu)}\right)\right) \quad (2.28)$$

$$p = \left(\frac{k_2}{k}\right)^2 \quad (2.29)$$

$$G_{su} = \rho\left(\frac{\omega}{k_2}\right)^2 \tag{2.30}$$

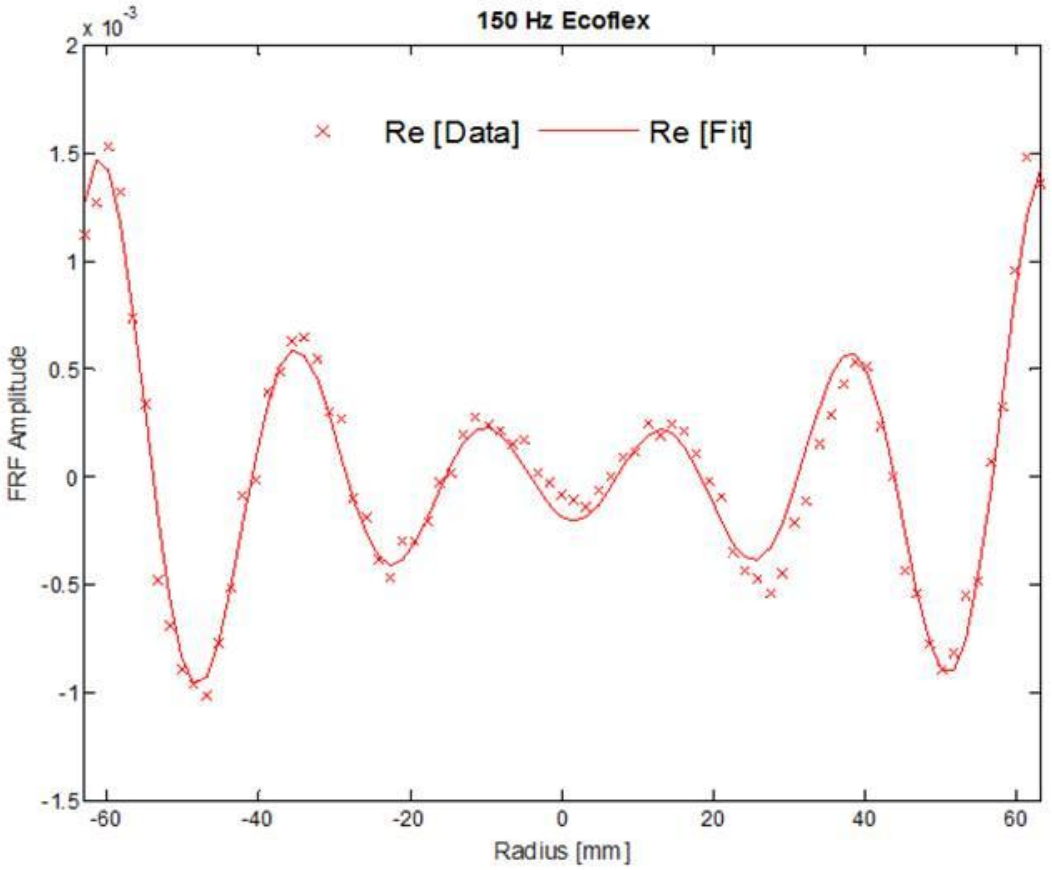

Figure 2-2: Real part of SLDV acquired amplitude Frequency Response Function (FRF) curve fitting example from the large diameter Ecoflex specimen at an excitation frequency of 150 Hz.

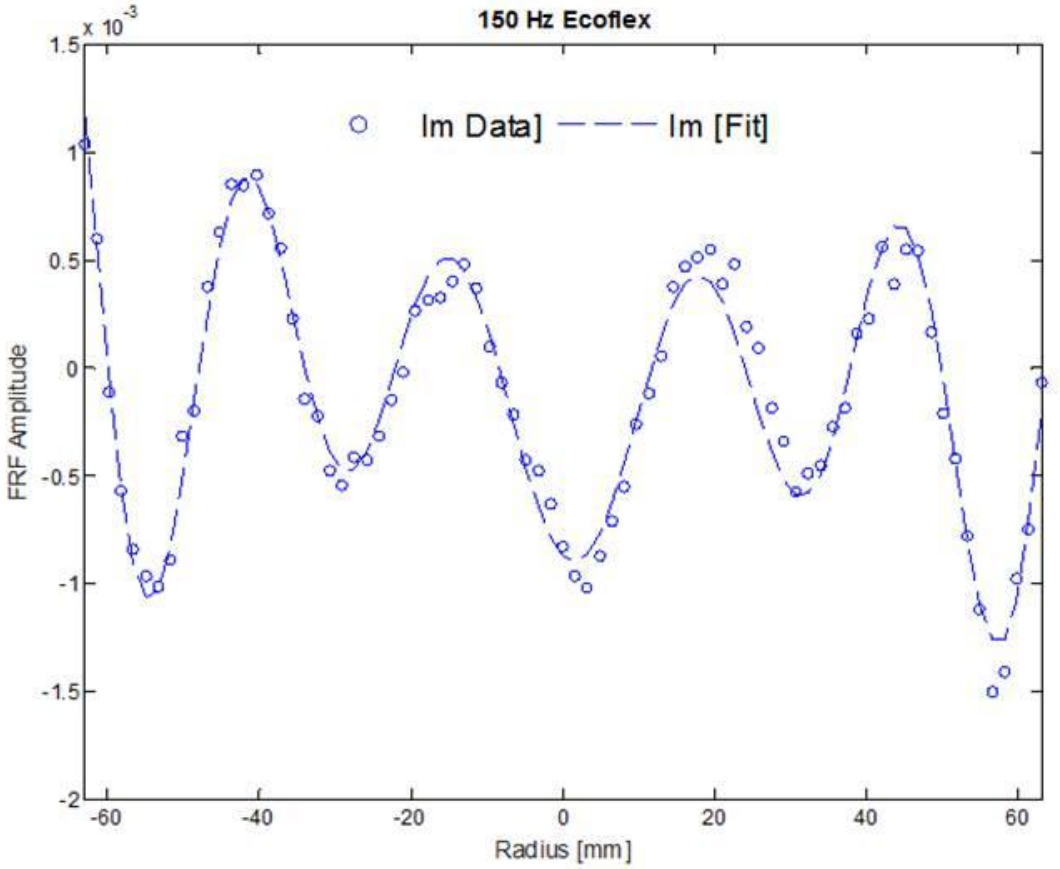

Figure 2-3: Imaginary part of SLDV acquired amplitude Frequency Response Function (FRF) curve fitting example from the large diameter Ecoflex specimen at an excitation frequency of 150 Hz.

CHAPTER 3

ELASTIC PHANTOMS AND SPECIMENS

This chapter contains details on how commercially available Ecoflex and Plastisol were used to create the elastic phantoms and specimens used in this thesis.

3.1 Ecoflex and Plastisol Preparation

Ecoflex and Plastisol are provided by the manufacturer in liquid form. Each has a shelf life of approximately one year. The benefits of the materials are that they can be casted or poured into various mold containers. Another is that the stiffness can be adjusted depending on the amount of softener added to the initial mold liquid. Preparation for Ecoflex is different from Plastisol. The following will give instructions on how the materials were prepared for use in all phantoms and specimens.

Ecoflex:

- "Ecoflex-0010" (Smooth-on)
- A+B (solidification 40 minutes after initial mixing).
- Always use an equal amount of A and B in calculation when adding softener.
- Softener is silicon brake oil (USA standard Dot 5 brake fluid, purple in color). Other silicon based oils may work, too.
- Stir very well before pouring liquid into mold before solidification.
- Smooth-on release agent can be coated onto mold surfaces (use specific product instruction).
- Cured Ecoflex will stick to surfaces not containing release agent.
- Evacuate bubbles with vacuum chamber before pouring.

- Room temp.
- Pour Ecoflex on paper plate to spread out surface area (will evacuate bubbles faster).
- Let sit for 24 hours (1 week for total cure).

Plastisol:

- "Liquid Plastic and Softener" (Alumilite Corporation)
- Comes looking milky white in factory container.
- Softener is added before heating.
- Heat until milky white turns transparent (can use microwave).
- MUST use safety glasses and high temperature glove for handling heated container.
- Evacuate bubbles in vacuum chamber while liquid is still hot (no more than 3 minutes).
- Scrape solidified bubbles off of top surface after vacuum chamber.
- Reheat in microwave if needed.
- Petroleum jelly can be coated onto mold surfaces for a Plastisol release agent.
- Cured Plastisol will stick to surfaces not containing release agent.
- Poor about 3/4's of heated liquid into new jar which will be used to poor into final mold (if you use original heated container, the bottom layer will contain contaminates).
- Never empty all liquid from container into mold (always make more than necessary for avoiding bottom container contaminates as the top layer experiences bubble solidification.
- Let sit for 24 hours (1 week for total cure).

3.2 Pressure Loaded Phantom

The pressure loading study uses a plastic 3.2 cm diameter cylinder x 4.0 cm in length filled with multiple internal stiffness layers of Ecoflex. The layers are a soft outer layer (annulus dimension = 1.5 cm), hard middle layer (annulus dimension = 1.3 cm), and a center void (0.4 cm diameter) for variable pressure loading with all layers contained in a thin walled plastic cylinder (Figure 3-1). The layers are created by systematically placing a large and small circular bar into the center of the plastic cylinder while waiting for each Ecoflex layer to solidify separately. Release agent from the Ecoflex manufacturer was used on the circular bars to ease the extraction from the solidified Ecoflex. No softener was added to the hard layer. The softer layer contains 13.3 % silicon brake fluid for softening. One end cap is glued with epoxy to the bottom end of the specimen before Ecoflex is added and the other is glued on after solidification. A plastic hose runs into the front end of the phantom for variable pressure control (Figure 3-2).

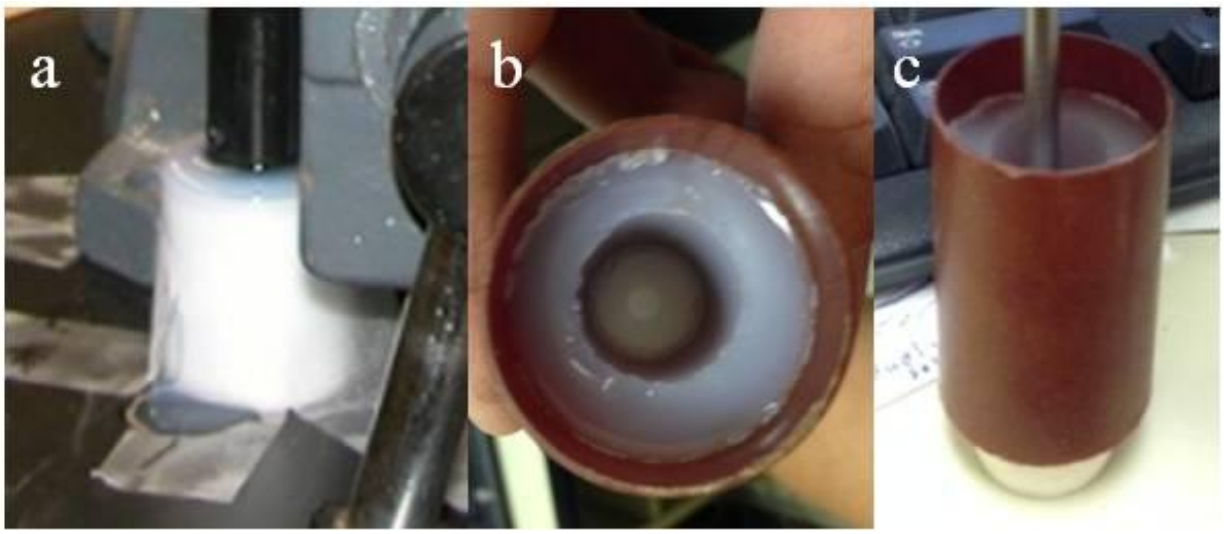

Figure 3-1: Construction of multi-layer Ecoflex phantom used in Phase 1 pressure loading study. (a) Large circular bar used to form outer layer. (b) Outer layer final solidification. (c) Small circular bar used to form inner layer.

Figure 3-2: Completed multi-layer phantom is shown placed in water for visual air bubble leak pressure testing before experiments.

3.3 Tensile Specimen

The dog bone phantom is created for the tension study in Chapter 6. Ecoflex 0010 was casted into a 2.54 cm diameter x 12.7 cm long cylinder with additional 3.49 cm diameter x 1.27 cm long cylinder ends. The 2.54 cm diameter specimen cast was bored from a 15.24 cm long x 3.49 cm diameter aluminum bar that was cut in half along the bar length to form two identical cast sections (Figure 3-3). Glue was used to seal the two cast sections together so no liquid Ecoflex leaked during the solidification process. Duck tape was also wrapped around parts of the cast sections to help hold them together during pouring and solidification.

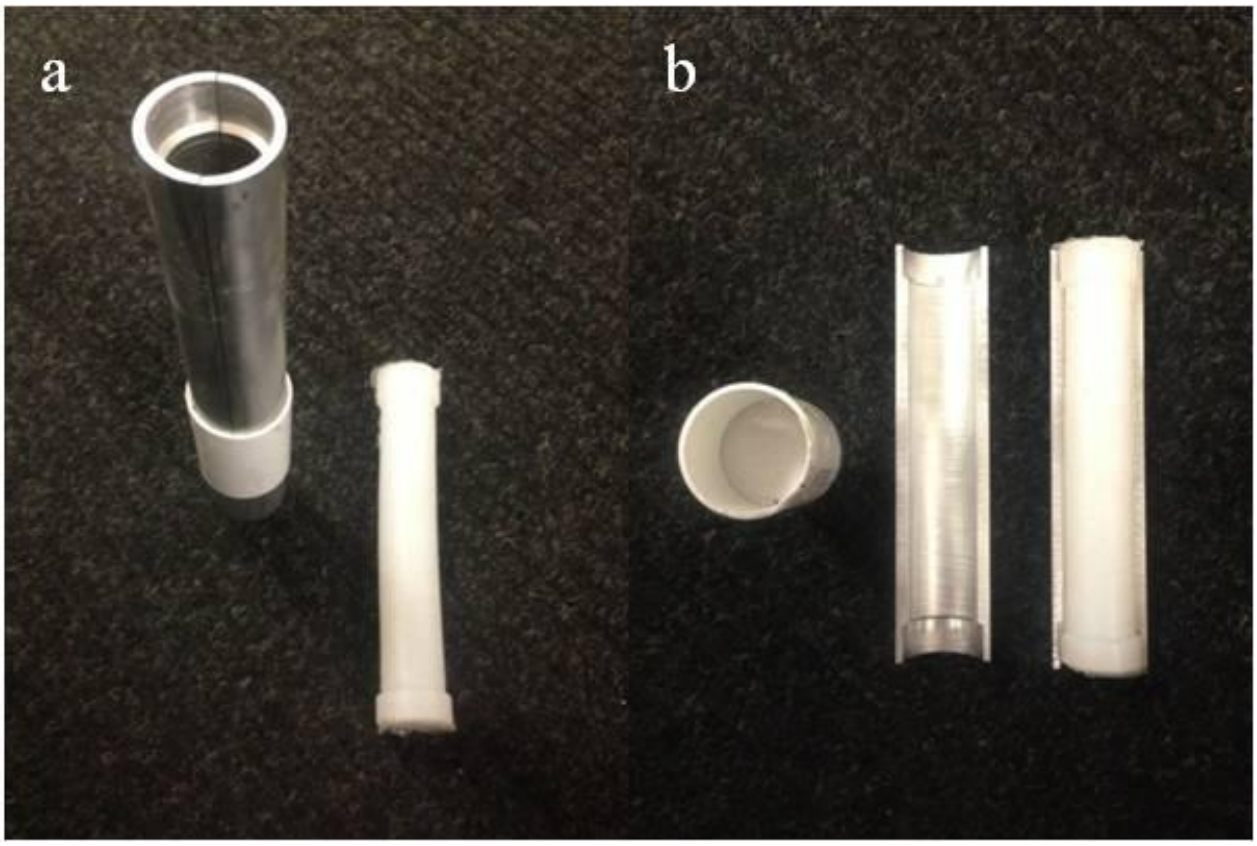

Figure 3-3: Cast used to mold tensile dog bone specimen. (a) Full cast ready for pouring mold with specimen also shown. (b) Two identical cast sections showing specimen shape machined from 15.24 cm long x 3.49 cm diameter aluminum bar and bottom cast holder; also specimen shown in one of the cast sections after solidification.

3.4 Optical Validation Cylindrical Specimens

Liquid Ecoflex and Plastisol with prepared for different stiffness were poured and then solidified in stock 5.5" and 2.5 ID x 3" thin walled acrylic cylinders (Figure 3-4). Circular disks were machined out of 1/2" thick acrylic plate and pressed into the cylinder front ends. A small edge (greater than the given cylinder inside diameter) in the form of a cap was left around each disk to keep the disks perpendicular to the cylinders once pressed in place. After the Ecoflex or Plastisol solidified, the disks were gently removed from the cylinders leaving both ends open. A very thin layer of petroleum jelly used as a release agent was placed on the disks flat surfaces before the liquid Ecoflex or Plastisol was poured in the

cylinders. The specimen surfaces on the pressed disk end were coated with reflective microbeads with refractive index greater than 1.93 and size = 35 to 45 microns (Cole Safety Products). Microbeads were found to enhance the laser reflection from the specimens.

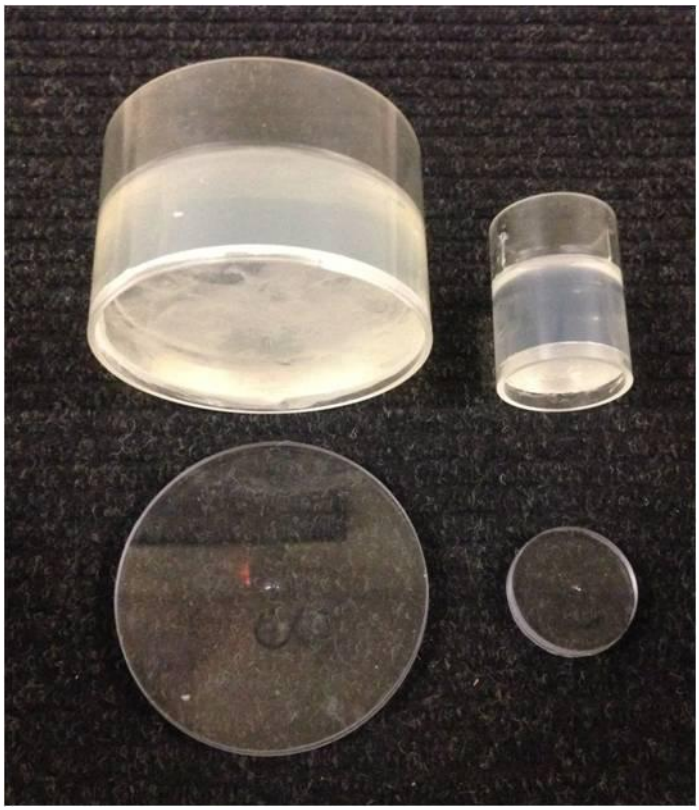

Figure 3-4: Cylindrical 5.5” and 2.5” specimens used for optical validation study. Plastisol is shown in image. Ecoflex was used in identical cylinders. The circular disks for the solidification process are shown removed below each corresponding cylinder.

CHAPTER 4

EFFECTS OF QUASISTATIC INTERNAL PRESSURE LOADS ON A MULTI-LAYERED PRESSURE VESSEL PHANTOM IN MR ELASTOGRAPHY

This chapter was presented as Brinker SB, Kearney SP, Royston TJ, Klatt D. Effects of quasistatic internal pressure loads on a multi-layered pressure vessel phantom in MR elastography. Proceedings of ICEM: 16th International Conference on Experimental Mechanics (Cambridge, UK, July 7 – 11, 2014)

4.1 Introduction

Diagnosing diseases, such as hydrocephalus, edema, and hypertension with tissue pressure measurement is in many cases invasive and does not represent the entire tissue ROI under investigation. MRE stiffness changes are related to tissue pressure. The potential for MRE in this regard is large since MRE is noninvasive and can assess the entire volume of the tissue ROI. However, pressure loading conditions are still not entirely understood when analyzing tissue pressure with MRE. The aim of this pressure loading study is to examine the capability of MRE to assess pressure related stiffness changes in elastic phantoms that represent simplified structures of organs.

Several studies have been conducted to investigate the effects of pressure loading in MRE analysis. The studies include ex vivo, in vivo, phantom, animal, and human experiments. Hirsch has performed MRE on in vivo human organs and found volumetric strain changes are linked to high and low pressure changes from the cardiac cycle, respiratory cycle, and shunt placement (Hirsch, Klatt, et al. 2013; Hirsch, Posnansky, et al. 2013; Hirsch et al. 2014). The lungs showed increases in average DV magnitude from inhalation to exhalation in 9 subjects from 7 to 78 % using 50 Hz oscillation (Hirsch, Posnansky, et al. 2013). In a liver study performed by Hirsch, 50 Hz oscillation MRE was performed on in vivo human livers pre and post transjugular intrahetatic portosystemic shunt placement. DV increased

with shunt placement in 13 subjects with an average relative change of (21 ± 13)% with p-value = 1.38 x 10^{-5} (Hirsch et al. 2014). Hirsch also performed MRE on human brain at 25 Hz oscillations during controlled cerebral spinal fluid pressures increase from abdominal muscle contraction. Another data collection method similar to MRE is called phase contrast MRI where phase image data was obtained at various increments during the cardiac cycle. Volumetric strain was calculated from the image data. Approximately 45% (P = 0.0001) increase in DV was seen in 8 subjects during abdominal muscle contraction. DV showed an average of DV of (2.8 + or – 1.9) x 10^{-4} in six subjects (Hirsch, Klatt, et al. 2013).

Yin obtained shear stiffness of in vivo porcine of liver and spleen where measured with MRE in relation to portal pressure. Left ventricle and portal catheters logged blood pressure during MRE scanning. Linear regression coefficients between liver and spleen stiffness related to increasing blood pressure was greater than 0.8 mmHg. Tissue stiffness increased with rising blood pressure (Yin et al. 2013). Kolipaka created a Wirogel silicon rubber heart-simulating phantom with a pressurized and flexible internal water bladder. MRE at 200 Hz oscillation recorded periodic motion of the phantom at multiple time points during 18 to 72 beats per minute of bladder pressure cycles with 55 to 90 mmHg. Shear stiffness increased and decreased in sync with bladder pressure with a linear correlation of R^2 of 0.98 between stiffness and pressure (Kolipaka et al. 2009). Hirsh conducted MRE on a pressure phantom containing a mixture of solidified ultrasound and water–agarose solution with a distribution of small internal air bubbles placed in a plastic cylinder. Scans were obtained for every individual pressure increment while the internal cylinder air pressure was increased from 0 to 4.8 bar by steps of 0.5 and then decreased to 0 bar until in steps of 1.0 bar. DV from 50 Hz MRE increased with rising pressure and decreased with pressure. A relaxation or hysteresis pattern could be seen in the DV relation to the pressure cycle (Hirsch, Posnansky, et al. 2013). Hirsh also conducted MRE on an excised sheep liver including a water inflow tube connected to the portal vein sealed with Wirogel. Raising a water reservoir above the scanner table to heights of 0, 20, 40, 60, and 77 cm for increasing pressure increased the

resulting MRE derived DV with reservoir height. There was no visible correlation between MRE shear stiffness and water pressure (Hirsch et al. 2014). However, Rajagopal showed that shear modulus of elastic material is dependent on static pressure in the form of a general analytical solution using results from an experimental study conducted by Paterson (Rajagopal 2009; Paterson 1964).

This project is designed to examine simplified structures of soft tissue that make up the brain, heart, and lungs. The project investigated MRE stiffness changes in elastic media with multiple stiffness layers. The goal is to see how the media structure influences MRE stiffness from internal pressure variation. The findings may better help understand what causes tissue pressure to change MRE stiffness and ultimately enhance the capability of MRE to diagnose pressure related disease symptoms.

4.2 Material and Methods

The study uses a cylindrical Ecoflex phantom made with a center void for variable pressure loading, a hard middle layer, and a soft outer layer contained within a plastic rigid plastic cylinder (Figure 4-1). MRI magnitude images show the phantom with air (Figure 4-2(a)) and liquid (Figure 4-2(b)) in the center pore space where the internal pressure is induced. Phantom construction details are highlighted in section 3.2 of Chapter 3. The phantom is cyclically loaded with four air cycles at 0, 50, 100, 150 mm/Hg and repeated with liquid loading via a 9.5 mm plastic hose. MRE scan times were approximately 6 minutes for each pressure increment and 1.5 minute intervals were taken between each scan for adjusting the air or liquid pressure to the next steady-state value. For each pressure increment, the shear modulus g_z was determined by applying a Helmholtz inversion to the temporally resolved MR phase images. Theory and post processing details for g_z can be found in section 2.1 and 2.2 of Chapter 2. The scan used a 2D spin echo MRE pulse sequence with parameters: TR = 200 ms, TE = 13.82 ms, motion encoding gradient cycles = 20 with gradient strength of 20 G/cm, f_e = 2 kHz, slice thickness = 2 mm, matrix = 128 x 128. An MRI compatible piezoelectric stack delivered approximately 2 microns of displacement and 2 kHz of

mechanical vibration to the phantom in the axial direction. The multilayer phantom is placed on an MRI insertion platform (Figure 4-3) where the piezoelectric (Figure 4-4) oscillates the phantom in a translation motion (Figure 4-5) parallel to the magnet bore length. The workflow to obtain the shear moduli for each phantom layer used magnitude MRI images to mask out the ROI for each layer (Figure 4-6(a)). Shear waves propagated fastest through the inner harder layer as seen by the longer wavelengths when compared shorter waves in the outer layer of softer media (Figure 4-6(b)). From the stiffness maps, a difference in g_z can be seen between the inner and out layers (Figure 4-6(c)). MRE data is acquired for each pressure increment to assess MRE stiffness with changing pressure. Pressure was continuously visually monitored by the static air gauge shown in Figure 4-7.

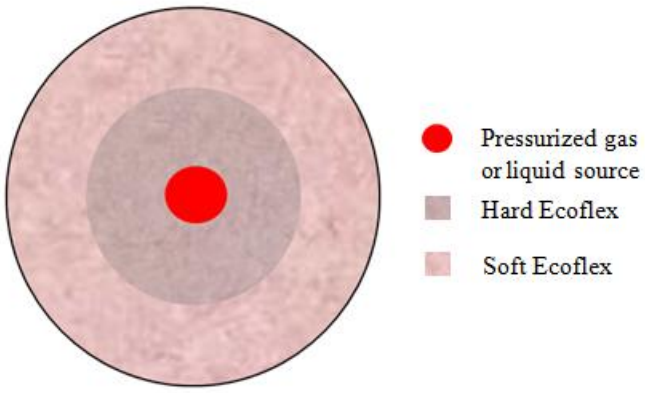

Figure 4-1: Ecoflex multi-layer phantom schematic with outer soft layer, inner hard layer, and inner pore for variable pressure loading source.

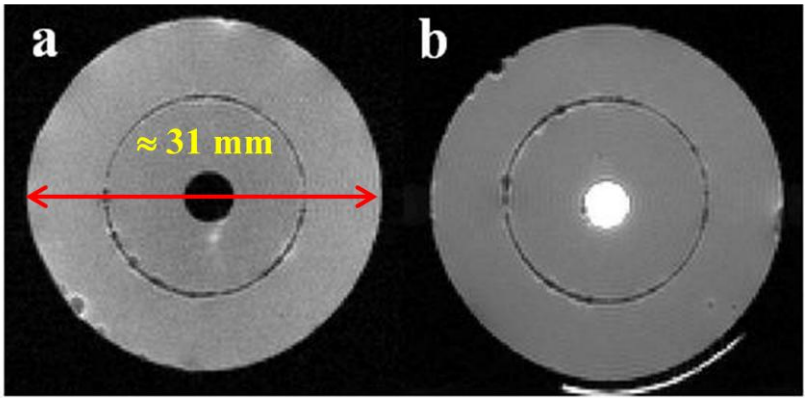

Figure 4-2: (a) Air filled pore in multilayer phantom for variable pressure loading. (b) Liquid filled pore.

Figure 4-3: Multilayer phantom mounted in MRI insertion platform and connected to piezoelectric actuator. Plastic hose inserts into phantom for pore pressure control.

Figure 4-4: Piezoelectric stack used to vibrate phantoms in MRE experiments.

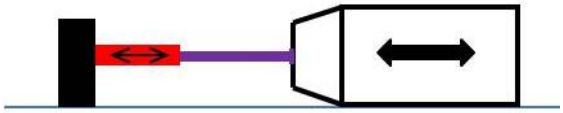

Figure 4-5: a) Translation actuation is induced into phantom by mounting it to a rod connected to a grounded oscillating piezo. The phantom slides freely on the MRI insertion platform.

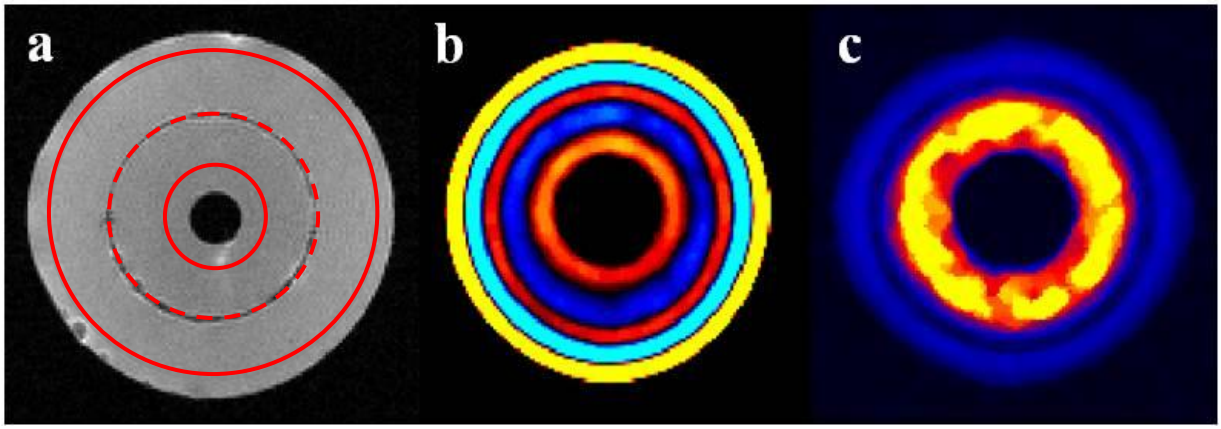

Figure 4-6: MRE workflow to calculate average shear modus for outer and inner layer of multilayer phantom with pore air pressure = 0. (a) Magnitude image used to segment each stiffness region used in processing data. (b) Example of wave propagation through phantom where the inner layer experiences longer wavelengths than the outer stiffer layer. (c) Shear modulus stiffness map with the outer layer of a different stiffness than the inner.

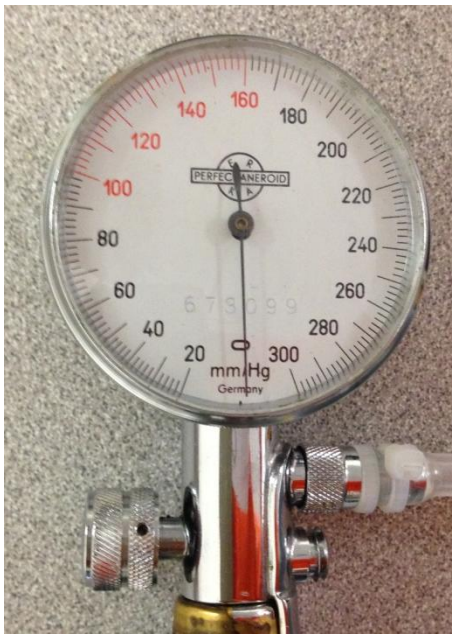

Figure 4-7: Pressure gauge used to monitor regulated pressuring loading into phantoms.

4.3 Results and Discussion

4.3.1 MRE Stiffness and Pressure Variation

A volume change in the phantom material is present in the MRE magnitude images of the phantom when taking the difference between maximum and atmospheric pressures images (Figure 4-8(a)). Figure 4-9 shows the data legend for plots in Figure 4-10, Figure 4-11, and Figure 5-12. The experimental results in Figure 4-10 indicate that internal air and liquid pressure changes influence the MRE derived shear stiffness values of both phantom layers. The numerical storage shear moduli values from the cyclic experiments categorized by scan order, timing, cycle, and pressures are listed in TABLE II. Vessel wall shear stiffness increases with internal pressure, however the pressure-stiffness curves and the pressure-amplitude curves (Figure 4-11) varied with pressure source and layer position. The most obvious region indicating hysteresis was observed in the outer layer stiffness values as liquid pressure was cycled shown in Figure 4-12.

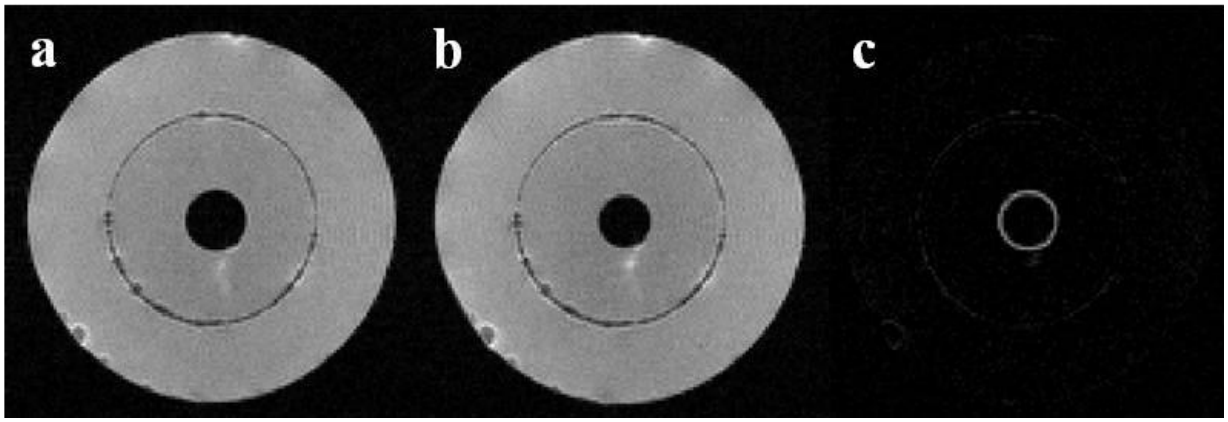

Figure 4-8: Phantom layers in compression from volume change due to internal pressure loading of air filled pore (a) Air pore at max pressure = 150 mm/Hg. (b) Air pore at atmospheric pressure = 0 mm/Hg. (c) “Image b” subtracted by “Image a” to visualize compression strain from the change in pore pressure.

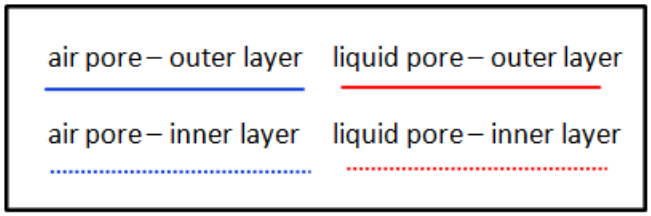

Figure 4-9: Data legend for plots in Figure 4-10, Figure 4-11, and Figure 5-12.

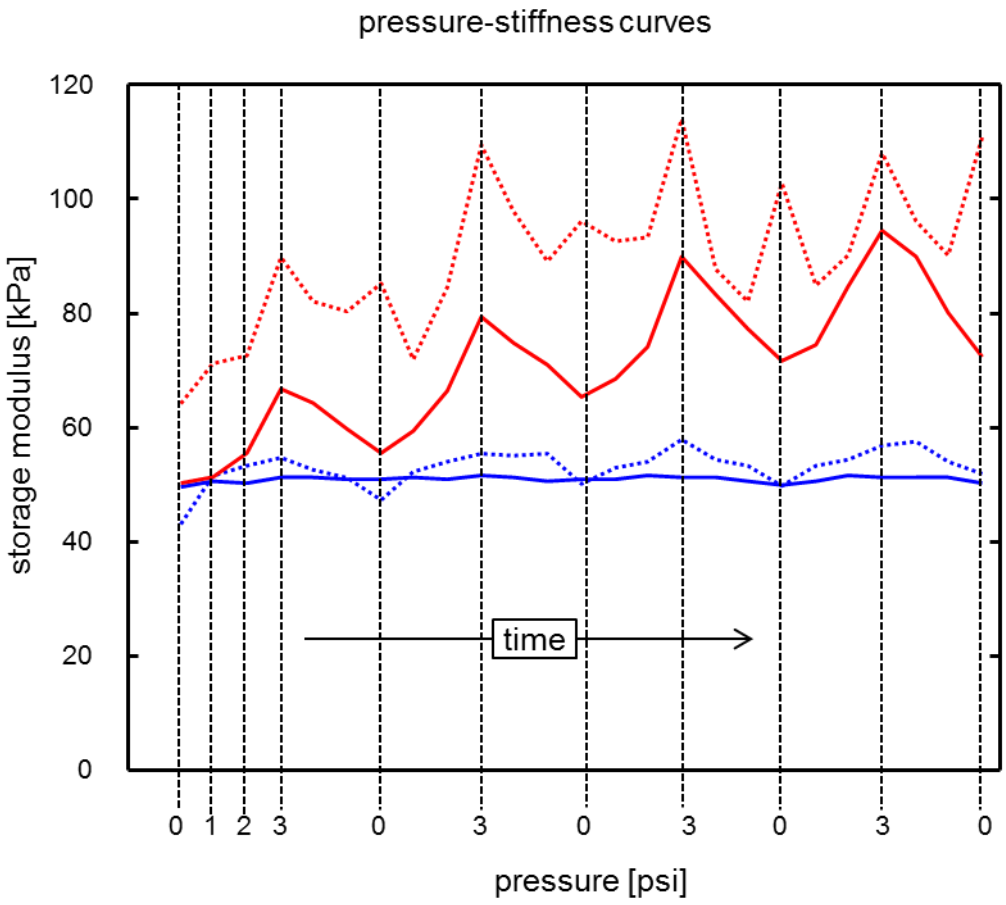

Figure 4-10: Average MRE shear modulus for each layer from the multilayer phantom over all 4 cycles during air and liquid pressure loading.

TABLE II
TIMELINE OF SHEAR MODULUS FOR MULTILAYER PHANTOM OVER 4 PRESSURE CYCLES

Scan #	Time (min)	Pressure (mm/Hg)	Cycle	$G_{air\ inner}$ (kPa)	$G_{air\ outer}$ (kPa)	$G_{liquid\ inner}$ (kPa)	$G_{liquid\ outer}$ (kPa)
1	0	0	1	43.02	49.22	64.08	49.95
2	7.5	50	1	51.42	50.19	70.94	51.08
3	15	100	1	53.16	50.10	72.52	55.40
4	22.5	150	1	54.44	51.01	89.49	66.39
5	30	100	1	52.36	51.05	81.92	63.87
6	37.5	50	1	51.14	50.81	80.13	59.55
7	45	0	1	47.30	50.71	85.04	55.38
8	52.5	50	2	52.06	50.89	71.82	58.95
9	60	100	2	53.93	50.86	84.52	66.01
10	67.5	150	2	55.29	51.45	109.34	79.00
11	75	100	2	54.82	51.15	97.66	74.39
12	82.5	50	2	55.28	50.19	89.02	70.58
13	90	0	2	50.04	50.80	96.06	64.96
14	97.5	50	3	52.90	50.71	92.58	68.17
15	105	100	3	53.99	51.45	93.20	73.78
16	112.5	150	3	57.82	51.07	113.97	89.53
17	120	100	3	54.36	51.04	87.52	83.03
18	127.5	50	3	53.21	50.29	82.04	77.04
19	135	0	3	49.77	49.67	102.66	71.37
20	142.5	50	4	53.24	50.43	84.89	74.16
21	150	100	4	54.38	51.30	89.86	84.48
22	157.5	150	4	56.82	51.09	107.95	94.29
23	165	100	4	57.39	51.09	95.93	89.54
24	172.5	50	4	53.75	51.08	90.08	79.86
25	180	0	4	51.66	50.15	110.69	72.09

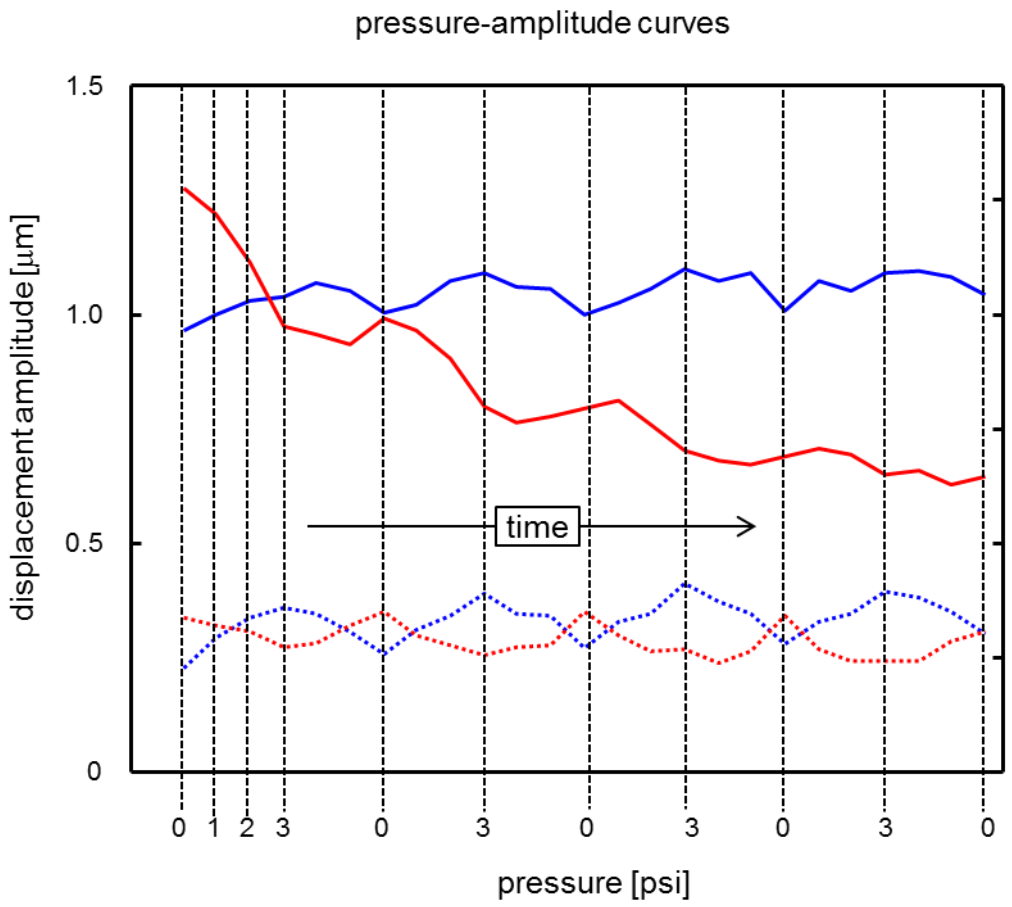

Figure 4-11: MRE displacement amplitude (perpendicular to the phantom axial direction) of inner and outer layers during air and liquid pressure loading in multilayer phantom.

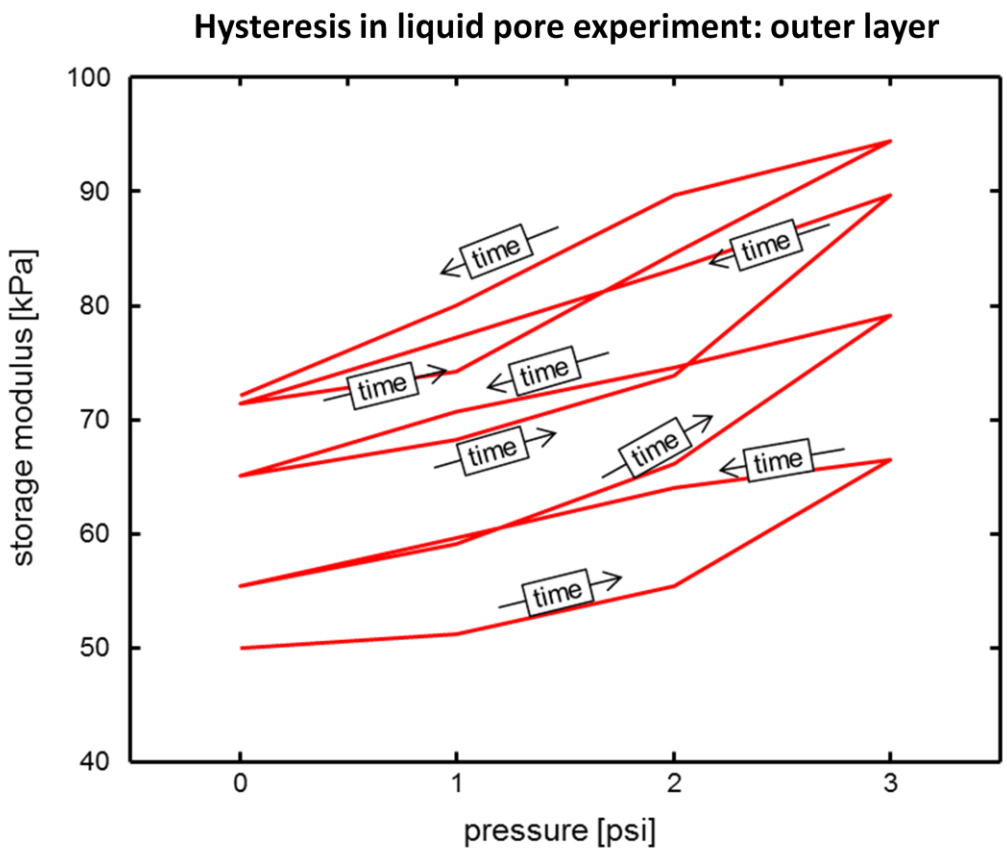

Figure 4-12: Hysteresis observed in the outer soft layer during 4 cycle of liquid pressure loading.

4.3.2 Comparison to Other Studies

All MRE phantom studies investigating pressure related stiffness resulted in increasing storage shear modulus with pressure. The experimentation from this study is in parallel with other pressure MRE phantom studies. One other phantom MRE study uses 1 cycle of pressure loading and indicates characteristics of hysteresis as pressure is returned to zero (Hirsch, Posnansky, et al. 2013). It becomes evident in the 4 cycles conducted in this study that hysteresis can be seen in the MRE stiffness. The 4 cycles were completed over a 180 minute period, which yields a significantly longer cycle period compared to a cardiac or reparatory cycle. Another study used a diastolic pump to simulate the cardiac cycle and still found the MRE derived stiffness to increase with pressure (Kolipaka et al. 2009). Though

hysteresis was not observed, it is most likely because steady state was reached after the first several pressure cycles. The studies using static pressure loading and this study are more relevant to understanding the tissue pressure-stiffness relationship in hydrocephalus and edema where internal pressure for the most part remains static. As indicated in human MRE stiffness pressure studies, pressure changes can be measured in the human body with MRE. Most of the studies used volumetric strain measurements that require acquisitions of 3D displacement fields in the ROI. However, only displacement fields perpendicular to the axial imaging plane where obtained during these experiments yielding only 2D MRE complex shear moduli values.

The goal of the study in Chapter 4 was to explore the influence of pressure on MRE stiffness. Built functional pressure phantoms were built to represent simplified versions of porous biological tissue. MRE stiffness increased with pressure loading. This opens the prospect to measure tissue pressure in hydrocephalus, hypertension, edema applications with MRE. Hysteresis was also observed, which suggests the viscoelasticity of soft material in Elastography is not only governed by dynamic damping of mechanical shear waves but also by static stress relaxation.

Acknowledgments

Funding source is NIH Grant # EB012142.

CHAPTER 5

CONSTRUCTION OF AN INTERCONNECTED POROSITY PHANTOM FOR STUDYING PRESSURE LOADING IN POROUS MEDIA WITH MRE

5.1 Introduction

Soft tissue can be modeled as porous media to better assess the ability of measuring tissue pressure with MRE derived stiffness. Porous media has been defined in different ways related to the type of porosity being investigated such as pore size, interconnected network pores, or isolated pores. The different types of porosity can be found to influence tissue pressure in multiple parts of soft tissue. For instance, interstitial fluid or cerebral spinal fluid is saturated within the porosity of brain, muscle, and other tissues. These pores tend to be distributed in a homogenous pattern throughout tissue media and can be in the micrometer size range. Blood vessels and lung air spaces are sometimes defined as a biphasic media, which are pores distributed in an interconnected network with pore sizes in the millimeter size range.

An MRE human study showed that MRE derived stiffness is sensitive to the structure of soft tissue (Sack et al. 2013). In related investigations, multiple approaches have been used to simplify porous or biphasic media through computer simulation and experimental methods. Computer modeling of MRE inversion methods have been used to simulate deformation in response to harmonic mechanical excitation for various sizes of interconnected porous media. Most studies did not use networked pores but the porosity still had connectivity to allow material saturation (Perri et al. 2009; Perrinez et al. 2010). Phantom experiments have also been conducted to explore MRE of porous material with different sizes of isolated pores distributed evenly over the ROI (Hirsch, Beyer, et al. 2013).

The goal of this subproject was to design and build a pressure phantom that has different sizes of interconnected porosity networks in controlled regions of the same media. A schematic of the phantom is

shown in Figure 5-1. From trial and error during the development of the multi-layer pressure vessel phantom in chapter 4, the porosity phantom design was conceived. The design will allow future investigations for studying how controlled gas and liquid pressure loading change MRE derived stiffness in different pore sizes.

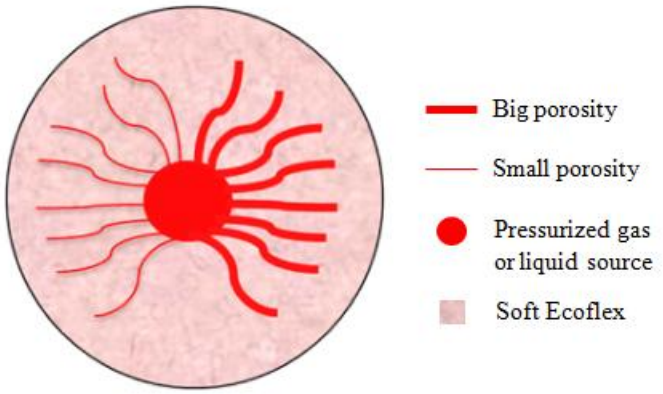

Figure 5-1: Ecoflex multi-layer phantom schematic with outer soft layer, inner hard layer, and inner pore for variable pressure loading source.

5.2 Interconnected Porosity Phantom Design and Construction

Two identical Ecoflex interconnected porosity phantoms with different stiffness were constructed. The hard phantom has no softener added and the soft phantom contains 25 % silicon brake fluid for softening. The interconnected porosity is made of webbed network channels that link to a center void for variable pressure loading. Each phantom has four sections of equal volume. The sections are an air filled small and a large pore region and a liquid filled small and large pore region. Every section from both phantoms is connected to the same pressure source. One rigid plastic cylinder contains a section of big pores and small pores made from extracting big and small copper wires out of a perforated copper tube and capped on each end by rigid plastic disks glued to the cylinder ends (Figure 5-2). One disk contains a plastic barb fitting that is mounted and glued in line with the center void for connection of a plastic hose for variable pressure loading. The other disk had a center hole with a plastic plug glued inside (Figure 5-2(d)). Wires were extracted from both sides of the phantom before the plug and barb fitting

were glued in place. Both ends of the perforated copper tube were used to hold the big and small wires. All successfully hold static air pressure in submerged water pressure testing.

Figure 5-2: (a) Big and small wires used for interconnected porosity network in phantom regions. (b) Wire network placed in rigid plastic cylinder. (c) Ecoflex solidification around wire network in cylinder. (d) Back side of cylinder with rigid plastic disk glued in place. (e) Additional plastic disk with barb fitting is glued onto other end of cylinder once wires and perforated copper tube are extracted from the solidified Ecoflex.

5.3 Image Analysis

High resolution MRI scans were performed on the two phantoms to visually gauge how well the porous networks remained after the Ecoflex cured and the wires were extracted. Figure 5-3 shows axial and coronal slices of the one phantom region of small and big pores. Larger pores can be seen on the right of the axial images and on the left of the coronal slices. Smaller pore regions are shown on the opposite side of the big pore regions. The small wire 0.53 mm in diameter and the big wire is 1.06 mm. Four times as much small wire length was used compared to the big wire length. The total wire amount in the small pore network has the same volume as the big pore network. This results in the small pore network having approximately two times the amount of surface area compared to the big pore network. All wires were distributed evenly by eyeball over the two halves of the cylinder.

Figure 5-4(a & b) show a 3D isometric surface of the phantom created from MRI magnitude image data. Images visually display separate regions of the small and big porous distributed networks

within the Ecoflex media. The phantom has similar spatial characteristics to an organ with air or blood vessel networks. All phantoms were constructed in this manner so both regions could be measured in the same MRE scan for simultaneous comparison. This phantom design will serve as a new potential method to investigate tissue pressure within porous media with different pore size using MRE. Stiffness correlated to pore size or distribution may be related to diagnosing tissue pressure symptoms concerning disease progression in soft tissue using MRE. The mechanical wave motion acquired from MRE traveling through the big and small pore regions can be seen in Figure 5-4(c). Figure 5-4(d & e) show a picture of the phantom and a schematic of how mechanical excitation is introduced to the phantom, respectively.

This project demonstrates the capability of building interconnected pores in a synthetic viscoelastic material of different pore sizes, which can be pressurized for studying the influence of internal pressure on porous structures similar to human organs using MRE.

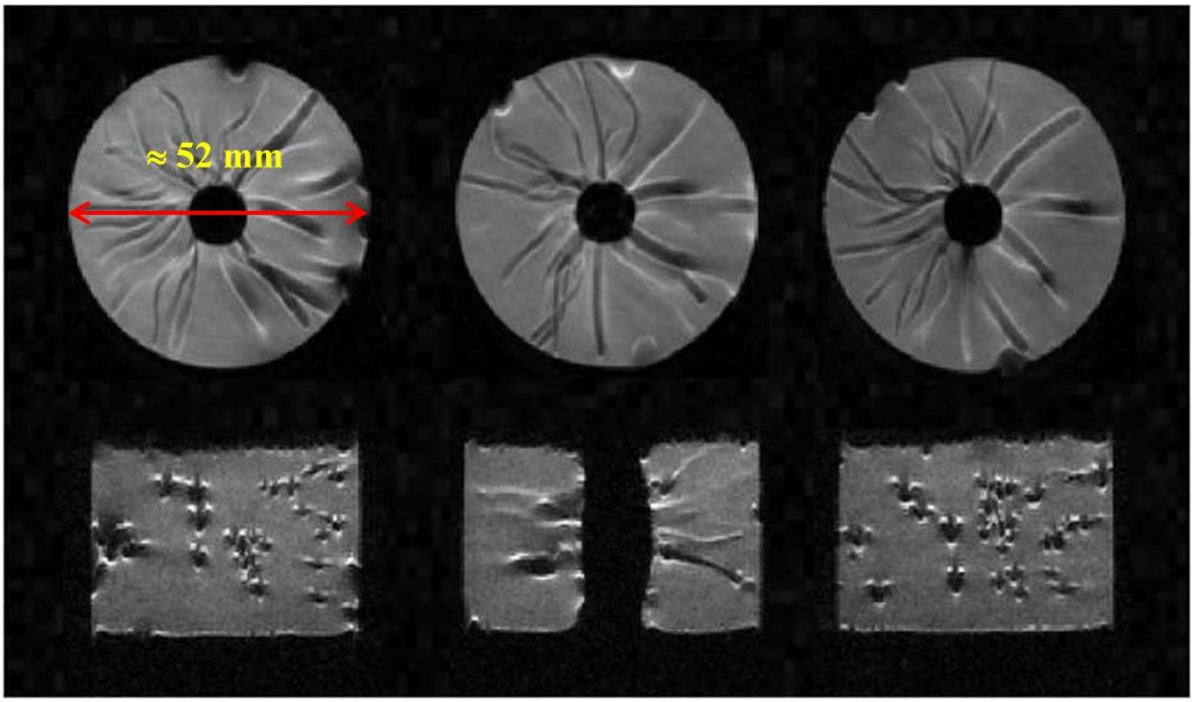

Figure 5-3: MRI magnitude images of one Ecoflex interconnected porosity phantom quadrant. Top row are axial images and bottom row are coronal slices.

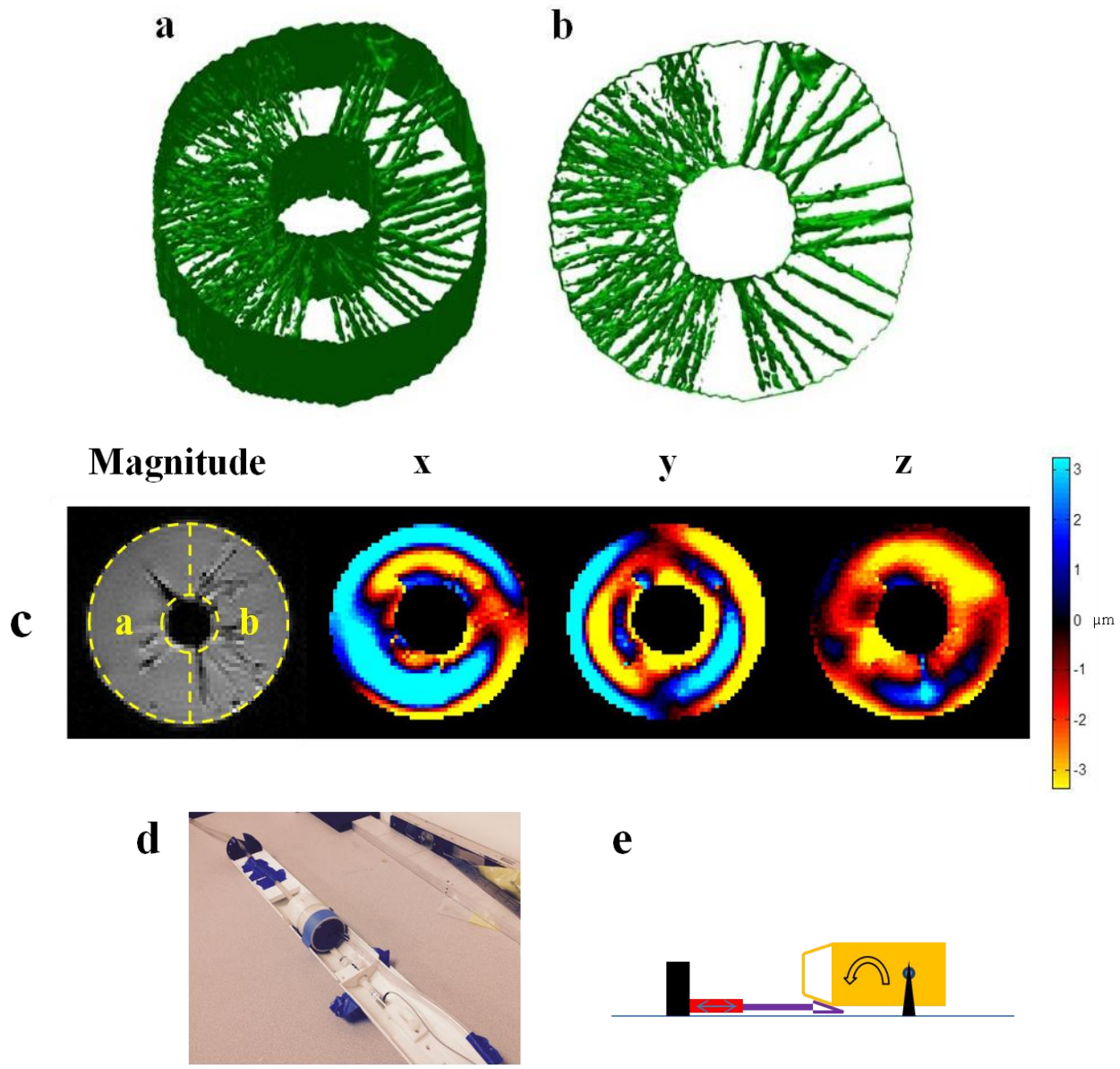

Figure 5-4: (a) Isometric surface produced from high-resolution MRI magnitude images of one interconnected porosity phantom quadrant. (b) Front view of isometric. (c) Axial images of the interconnected porosity phantom. The magnitude image, wave *x*-motion, *y*-motion, and *z*-motion are displayed from left to right, respectively. The areas within the yellow dotted lines drawn on the magnitude images represent the big pore region and the small pore region indicated with a yellow "a" and "b", respectively. (d) Picture of phantom. (e) Description of rotational motion used for phantom mechanical excitation (phantom in yellow).

Acknowledgments

Funding source is NIH Grant # EB012142.

CHAPTER 6

DEMONSTRATION OF CONCURRENT TENSILE TESTING AND MAGNETIC RESONANCE ELASTOGRAPHY

This chapter was submitted (first submitted on January 2016,) as Spencer Brinker, Dieter Klatt, "Demonstration of Concurrent Tensile Testing and Magnetic Resonance Elastography", Journal of the Mechanical Behavior of Biomedical Materials.

6.1 Introduction

MRE measurements provide quasi-quantitative information because several subjective assumptions and image processing parameters ultimately influence the estimated stiffness values. Currently, no formal standard for post processing of MRE data exists. However, there has been an effort to validate MRE as a quantitative method by contrast to other material testing methods. Mechanical compression tests and dynamic shear testing of agar gel specimens have been compared with shear moduli obtained from MRE concluding correlation values of $R^2 > 0.99$ (Hamhaber et al. 2003; Ringleb et al. 2005). Stiffness from oscillatory rheometry of liver tissue was compared with multifrequency MRE. Various liver tissue types showed a similar shear modulus dependency on frequency while the absolute value of the complex shear modulus varied with temperature (Klatt, Friedrich, et al. 2010). A series of phantoms were measured for shear stiffness estimation using MRE and ultrasound elastography. The comparison showed a linear correlation of $R^2 = 0.93$ (Oudry, Chen, et al. 2009). A cross validation review for assessing liver fibrosis using ultrasound elastography and MRE concluded that each modality has good diagnostic performance. However, the study emphasized that standardization techniques are needed across elastography modalities so that different hardware and processing approaches produce similar quantitative results (Tang et al. 2015).

The accuracy of material testing methods that attempt to validate MRE depends on the experimental conditions, such as temperature and timing. Mechanical characteristics of soft materials, such as agarose and biological tissue, change with temperature (Chmarra et al. 2013; Klatt, Friedrich, et al. 2010). The concurrent acquisition of data using MRE and a corresponding validation method may help to minimize errors from time and temperature dependent stiffness changes.

MRE and force output measurements have been acquired at the same time for the purpose of studying muscle contraction related stiffness changes. MRE shear stiffness was found to increase from 2.68 ± 0.23 kPa during quadriceps relaxation to 3.87 ± 0.50 kPa with contraction (Klatt, Papazoglou, et al. 2010). Subjects in one study resisted torque against forward ankle rotation while MRE was performed on the tibialis anterior and gastrocnemius muscles. Shear stiffness in the muscles increased with torque load (Basford et al. 2002). Ex-vivo bovine and in-vivo human biceps brachii muscles were examined with MRE during tensile loading. Shear stiffness increased both with passive and active loading (Dresner et al. 2001).

The effect of tensile testing on internal material structure has been examined using X-Ray Computed Tomography (CT). Bovine cortical bone was placed in a micro-CT system to study the evolution of strain during tensile loading (Singhal et al. 2013). Aluminum alloy specimens were placed under static tensile loading while internal damage was observed by CT at stresses immediately before specimen failure (Hirano et al. 1995). The aim of the presented study is to investigate the influence of pre-tension on internal material structure represented by MRE derived stiffness, which is relevant to the analysis of voluntary muscle activation. Additionally the proposed tensile testing and MRE design may serve as a tool for MRE standardization by means of post-processing parameter optimization.

6.2 Materials and Methods

6.2.1 Specimen

Ecoflex 0010 was casted into a 2.5 cm diameter x 12.7 cm long cylinder with additional 3.5 cm diameter x 1.3 cm long cylinder ends. The mechanical behavior of Ecoflex tends to yield a linear stain limit close to 30 % at a strain rate of 50 mm/min with an initial dumbbell specimen length of 30 mm in tension (Franculli 2013). Whereas, some soft tissues experience lower linear strain limits below 2.6 % strain at frequencies of 5 to 350 Hz during oscillation mechanical testing in tension (Chatelin et al. 2010). It is common to consider both Ecoflex and soft tissue during mechanical testing as incompressible, homogenous, isotropic and a density close to water.

A cylindrical specimen geometry was used to maximize the amount of material in the MRI RF antenna. The specimen cylinder ends were pressed by hand through 2.9 cm OD, 1.9 cm ID plastic pulling rings that are both tied 3 times in an equilateral triangle pattern to pulling strings. Rings were used in this manner to distribute pulling force evenly over the specimen cross sectional area. The pulling ring ID is purposely made smaller than the relaxed specimen diameter in order to maintain gripping as the specimen diameter decreases in response to the large increments of longitudinal deformation. One end of the string was attached to a load cell mounted on an adjustable slide used to elongate the specimen along the axial direction while the other pulling ring remained statically grounded. The specimen length at unstressed state was 12.7 cm and the maximum stretch length was 30.5 cm corresponding to a strain of 140 % (Figure 6-1).

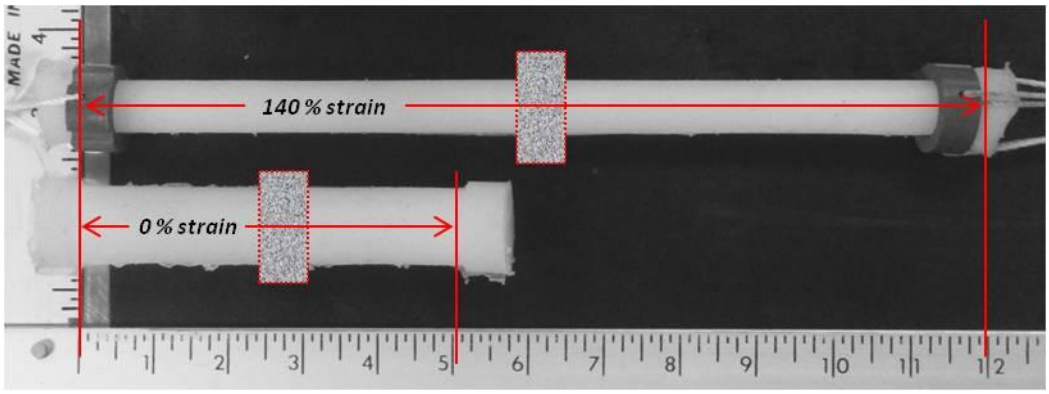

Figure 6-1: Ecoflex specimen used for simultaneous tensile testing and MRE. The red dotted line rectangles depict the approximate locations of the imaged regions.

6.2.2 Tensile-MRE Probe

A Tensile-MRE probe was custom-made, which elongates the specimen and measures tensile force while simultaneously introducing mechanical vibrations into the specimen. The probe has several components and functions to permit tensile testing during MRE data acquisition in the confined imaging area within a 3.9 cm ID RF birdcage coil, which has to be positioned in the center of the MRI bore of 172 cm length. Controlled stretching, measuring tensile force, mechanical excitation, gripping at multiple specimen diameters, and centering the image plane are the main functions incorporated into the probe design. The probe components are displayed in Figure 6-2 and Figure 6-3. Table V in the appendix lists all the materials used to build the Tensile-MRE probe by specification, function, and supplier. Of note, in addition to the components illustrated in the Figure 6-3 power cables for piezoelectric control and a plastic hose air line for actuator grip pressure control are contained within the probe. A transparent polycarbonate tube acts as the housing for the probe components within the magnet while the strain control slide rail contains an elongation slide and load cell. The tube and rail are bolted together and act as a rigid body. The pulling strings connected to each end of the specimen are routed unrestricted through the center of every probe component. A cap is embedded into the probe front end where the static pulling

string is grounded. The load cell was moved along the slide rail and locked in place to achieve different longitudinal strains.

The Actuator Grip Mechanism (AGM), which is illustrated in Figure 6-4, uses four grips to clamp around the center of the specimen. Two piezoelectric stacks mounted in parallel are connected in series with the AGM and are responsible for transferring mechanical vibration to the specimen when the grips are clamped. Static hydraulic air pressure delivered via two plastic syringes (3 ml) placed in parallel causes the distance between the grip collars to decrease until the four grips clamp the specimen (Figure 6-4(d)). Grips are unclamped by releasing the pressure in the syringes. The AGM was strategically adjusted to clamp onto the varying specimen diameter. Three different grip sizes (small, medium, or big) were used depending on the specimen diameter (the diameter decreases with increasing tensile elongation) as listed in Table I. There are four identical grips for each grip size. The probe was removed from the magnet to change grip sizes without specimen elongation being interrupted. Constant grip contact pressure for every specimen diameter was obtained by maintaining constant static air pressure in the syringes.

To accommodate the space necessary for maximum stretching the actuator sleeve is 35.6 cm in length. As a result of stretching the specimen at one end, it moves away from both the AGM and magnet center. The Tensile-MRE probe was designed to compensate for this misalignment. The piezoelectrics are mounted to an aluminum locking head with one end beveled. Figure 6-2(d) shows a beveled ram connecting to a locking rod as it screws into the beveled end of the locking head. Tightening the locking rod expands the ram against the probe housing and ensures the piezoelectrics are rigidly grounded during mechanical excitation. The entire MRE actuator system can slide freely around the tension string and specimen when the locking rod is loose and the AGM is unclamped around the specimen. Once the AGM is aligned with the specimen center and the grips are clamped, the entire probe is inserted further into the magnet to realign the specimen center with the magnet center. This process is repeated at each deformation state.

6.2.3 Experiments

The Ecoflex specimen was elongated to 0, 20, 40, 60, 80, 100, 120, and 140 % strain. Longitudinal tensile force and MRE scanning were acquired simultaneously during the specimen elongation. MRE scans of 1.5, 2.0, and 2.5 kHz mechanical actuation were performed consecutively at each strain using a preclinical 9.4 T MRI system (Model 310 mm Bore Actively Screened Magnet System Agilent Technologies, Research Products, USA). Tensile force was recorded once at the beginning of each MRE scan. The Tensile-MRE probe described in Section 3.2 was used for measuring the longitudinal tensile force, controlled stretching, and introduction of mechanical vibrations into the specimen. The vibrations generated by the two piezoelectrics were powered using an external amplifier, DC supply, and function generator. The piezoelectric control components were synchronized with the MRI system. MRE was performed using a SLIM pulse sequence (Klatt et al. 2013) with parameters: TR = 260.0 ms, TE = 26.6 ms, 30 cycles of the motion encoding gradients with amplitudes of 30 G/cm, 8 phase offsets (each twice with inverted gradient polarity), 8 axial slices of 2 mm thickness, matrix size = 96 x 96, field of view = 30 x 30 mm, and scan time was approximately 7 minutes. Additionally, 5 minutes was used to adjust the probe in between strain increments and 10 minutes to change grip sizes.

In order to examine the influence of the grip contact pressure on the MRE-derived stiffness, a set of 5 scans at f = 2.0 kHz and 140 % strain were performed consecutively using contact pressures of 1.4, 2.1, 2.6, 3.4 and 4.1 bar.

6.2.4 Data Processing

Tensile stress, T, is calculated using (2.18). The Fung model tensile stress, T_{Fung}, from (2.25) was fitted to the experimental T and strain using a nonlinear least-squares Levenberg-Marquardt algorithm for determining G_{inft} and b. The fitting was completed using the *nlinfit* function in MATLAB (Seber & Wild 2003).

ROIs were manually masked for each slice as shown in the magnitude images of Figure 6-6. At each phase offset, phase-difference images were calculated to filter contributions of static field inhomogeneities. The complex wave images were taken from the 1st harmonic after Fourier transformation of the temporally-resolved phase images and plugged into (2.12) to calculate the complex moduli of the first and second Lame-parameter, L and G. Prior to both 2D and 3D inversions, the complex wave images were filtered using a spatial Butterworth band pass filter with a lower limit of 6 pixels and upper limit using half of the field of view. G and L were spatially averaged over the two central slices in order to prevent edge effects and excluded outliers > 200 kPa. MRE frequency information of the spatially averaged G were linearly interpolated towards f = 0 Hz resulting in a G_0 for each strain increment. The normalized shear storage modulus $G_n(f, \varepsilon)$ from (2.16.a) was correlated with $T(\varepsilon)$ from (2.18) using Spearman's rank correlation for each excitation frequency and interpolated f = 0 kHz.

Finally, a 2D inversion from (2.15) was applied to each displacement direction of the complex wave images. To be consistent with the 3D approach, the complex shear moduli were spatially averaged over the two central slices while excluding outliers > 200 kPa resulting in g_x, g_y and g_z. An amplitude weighted G^* from (2.16) was then calculated for all strains and frequencies.

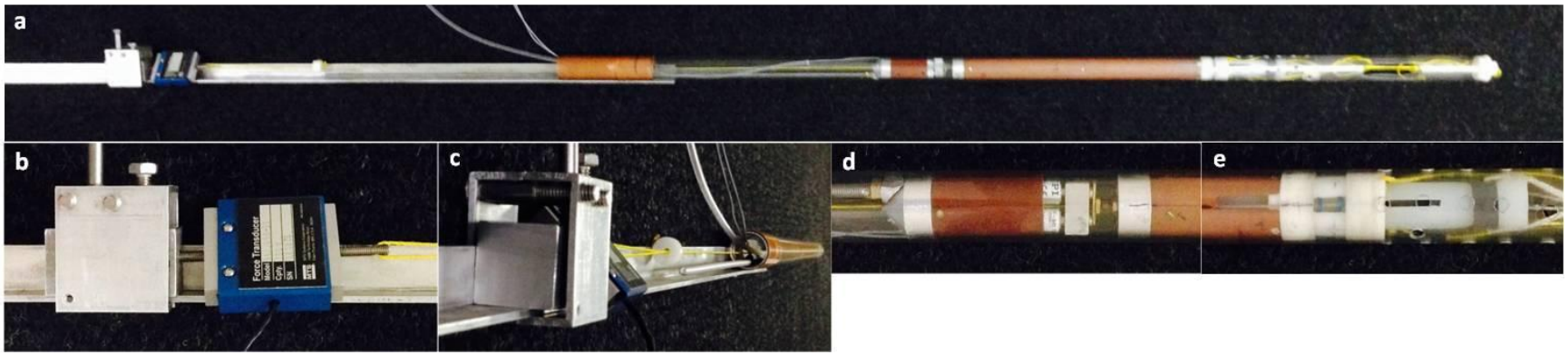

Figure 6-2: Photos of Tensile-MRE probe and components. (a) Full view of probe with 213.4 cm length and 3.8 cm outside diameter. (b) Load cell attached to elongation slide. (c) View looking down the center of the probe showing the actuator locking rod. (d) Two piezoelectrics placed in parallel attached to the beveled locking head and ram. (e) Actuator grip mechanism.

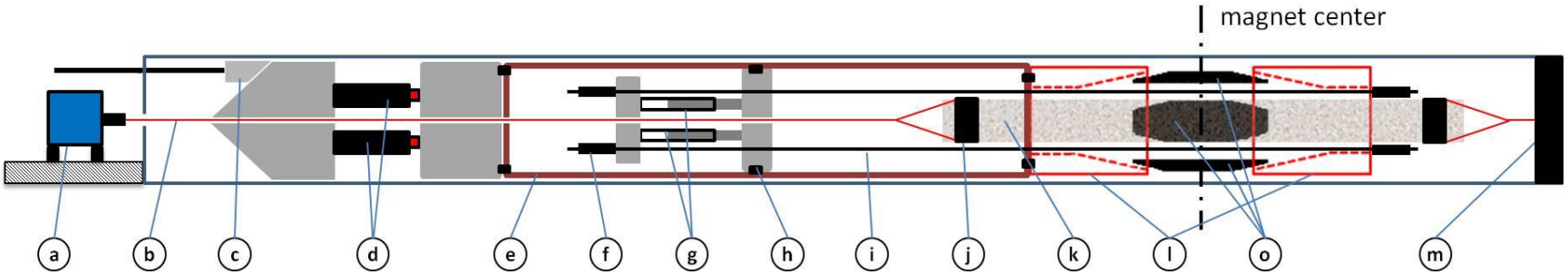

Figure 6-3: Schematic of Tensile-MRE probe internal components. All components sit inside a transparent polycarbonate tube. (a) Load cell mounted on adjustable elongation slide. (b) Tension string. (c) Locking head. (d) Piezoelectric actuators. (e) Actuator sleeve. (f) Heat shrink tubing. (g) Air syringes. (h) Mounting screw. (i) Tension rod between air syringe extension and grip collar compression. (j) Pulling ring. (k) Ecoflex 0010 specimen. (l) Grip collars. (o) Grips. (m) Probe end cap.

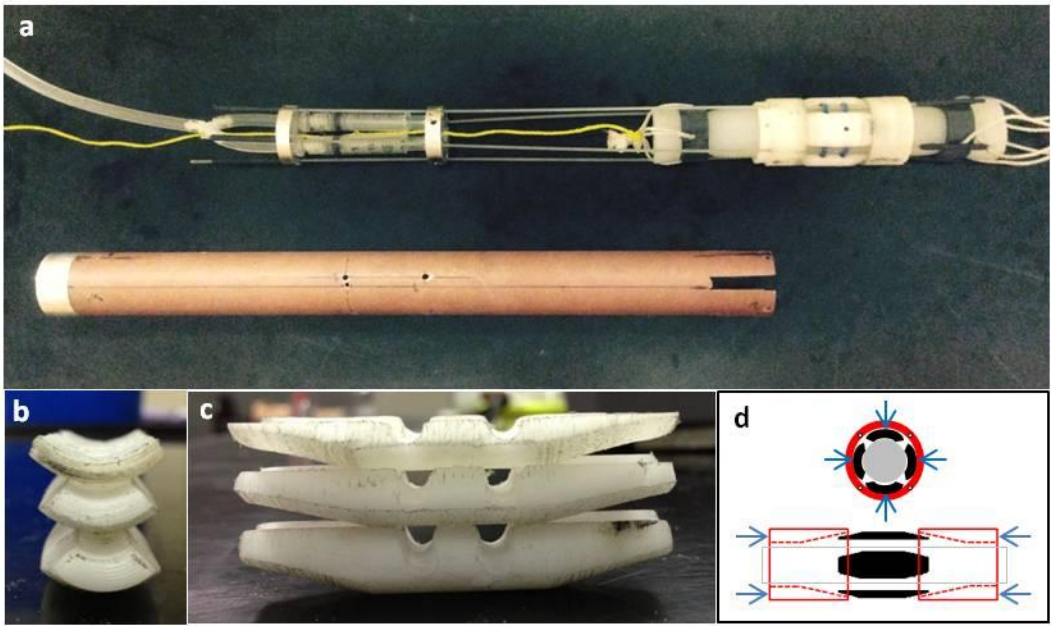

Figure 6-4: Actuator grip mechanism. (a) Actuator sleeve removed to show AGM internal components. Two air syringes transfer a closing tension to the grip collars through four garolite rods. (b) Front view of grip sizes with small, medium, and big on top, middle, and bottom, respectively. (c) Side view of grip sizes in same order as image b. (d) Depiction of grip collars and beveled grips used to transfer longitudinal expansion motion of syringes to radial clamping motion around the specimen.

6.3 Results

6.3.1 Pre-Test: Varying Grip Pressure

The results from assessing the influence of the grip contact pressure on the MRE-derived parameters are illustrated in Figure 6-5. The measurement using 3.4 bar provides sufficient vibration amplitudes with modest variation of the storage modulus in the pressure neighborhood. Therefore, the static air pressure in the syringes was kept constant at 3.4 bar through all further experiments.

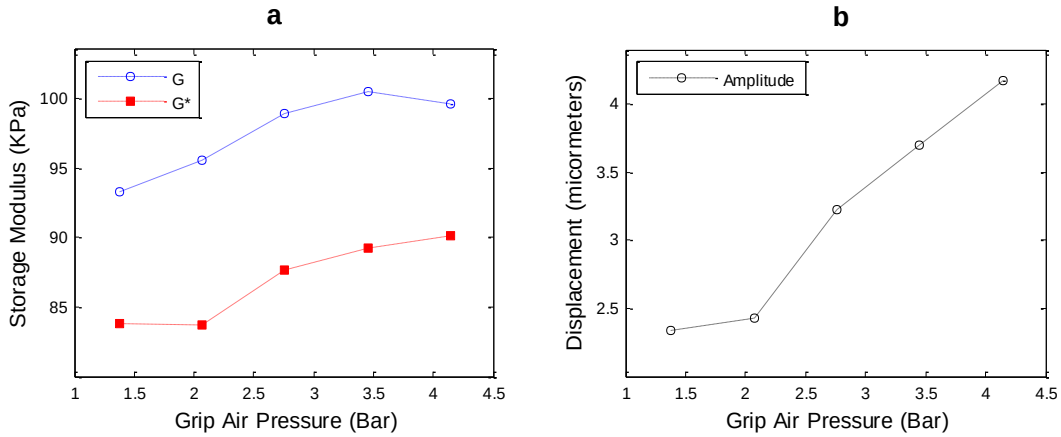

Figure 6-5: ROI-averaged values of MRE-derived (a) 3D shear storage modulus and (b) displacement using f = 2.0 kHz and 140 % strain. The grip air pressure was increased in increments of 0.7 bar (corresponding to approximately 10 psi).

6.3.2 MRE in Tension

Figure 6-6 shows a series of images processed to determine MRE shear storage modulus values at 0 and 140 % strain. The specimen edges squeezed by the actuator grips seen in the magnitude images are left out of the masked ROI, which is demarcated with dashed lines. The elongation of the specimen results in a reduced cross sectional area. Also the increased stiffness at 140 % strain compared to 0 % is indicated by longer wavelengths in the wave motion images and is clearly visible in the calculated G-map. Figure 6-7 displays ROI-averaged storage and loss modulus values for G and G^* vs. ε at various frequencies. Both storage and loss moduli increase with excitation frequency for the majority of deformation states. There is the trend that the storage moduli increase with the pre-tension, whereas the loss moduli seem to be less dependent on pre-tension. The comparison between shear storage moduli (Figure 6-8(a)) shows that g_z derived from scalar inversion is most similar to G obtained from full 3D vector field inversion. The z-directional component contributes to most of the G^* summation whereas the x- and y- components do not due to their lower vibration amplitudes (Figure 6-8(b)).

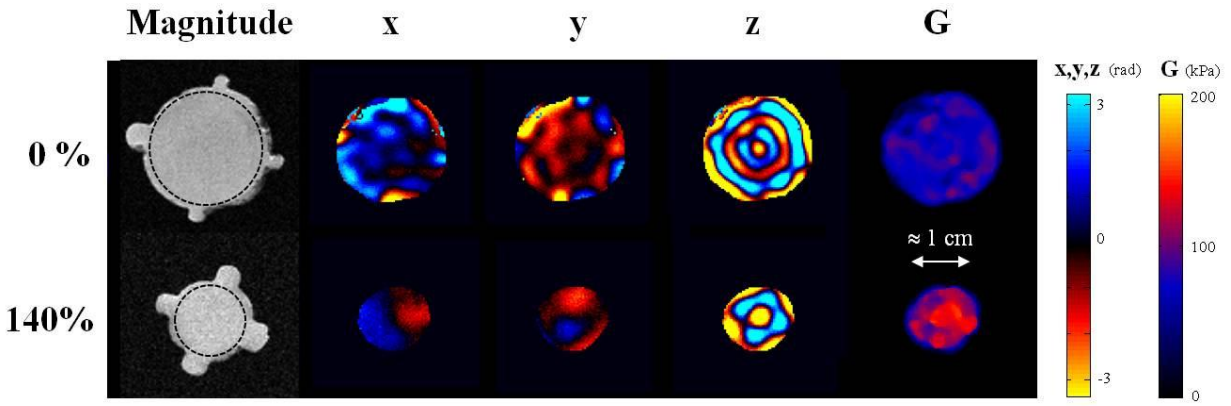

Figure 6-6: Axial images of a central slice for specimen at 0 and 140 % strain and using f = 2.0 kHz. The magnitude image, wave *x*-motion, *y*-motion, *z*-motion, and *G* stiffness map (shear storage modulus) are displayed from left to right, respectively. The areas within the black dotted lines drawn on the magnitude images represent the masked ROIs used for all image post processing and averaging. Separate ROI masks were constructed for each strain increment to match the changing specimen diameter in response to elongation. Wave motion represents displacement perpendicular to image plane.

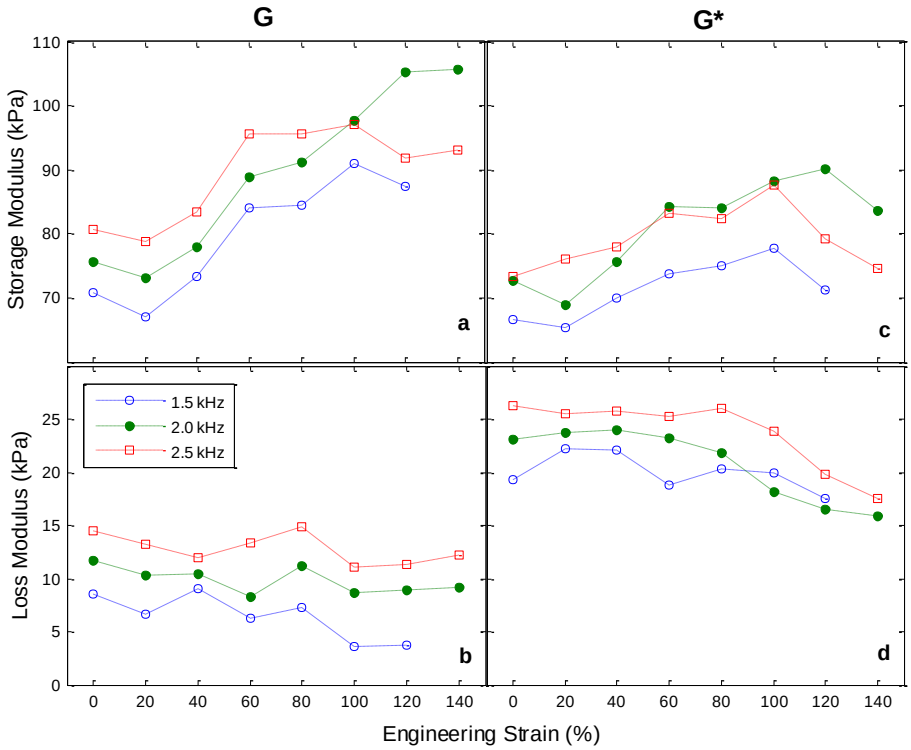

Figure 6-7: MRE-derived complex shear modulus in the strain range 0 to 140 % for f = 1.5, 2.0, and 2.5 kHz. (a) *G* storage modulus vs. strain. (b) *G* loss modulus vs. strain. (c) *G** storage modulus vs. strain. (d) *G** loss modulus vs. strain. *Of note, the complex shear modulus at 140 % strain with f = 1.5 kHz is considered an outlier and not displayed in the figure.

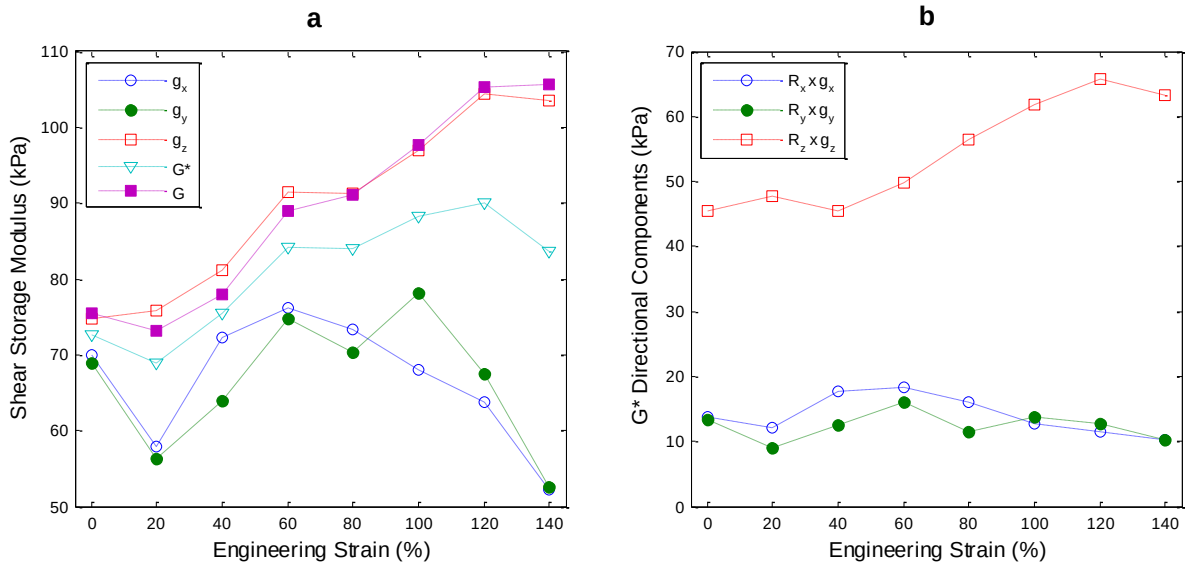

Figure 6-8: Comparison between 2D and 3D inversion shear storage moduli at f = 2.0 kHz. (a) G, G^*, g_x, g_y, g_z, vs. strain. (b) G^* directional components vs. strain.

6.3.3 Tensile Stress and MRE Comparison

Table III contains shear storage modulus G values for all excitation frequencies at each respective state of deformation. G_0 corresponds to the static modulus at f = 0 kHz that is interpolated from the frequency dependent moduli for each strain. Grip sizes used for each stretch length are also listed. The value of the shear storage modulus at ε = 140 % and f = 1.5 kHz is below its value at 0 % strain and results in a negative G_0 after interpolation. These values (denoted with a star (*) in Table III) are considered outliers and therefore not included in further analysis. Figure 6-9(a) displays G_n for all excitation frequencies and G_0 plotted against T for all strains. Of note, the normalized shear storage modulus G_n can be negative because of the subtraction of the value in the undeformed state from (2.16.a). Table IV lists all correlations for Spearman's rho and p-values between experimental tensile stress T (ε) and normalized shear storage modulus G_n (f, ε). Figure 6-9(b) shows experimental stress T, the fitted Fung model stress T_{Fung}, and G_n at f = 0 kHz (interpolated) vs. strain. Fitting the experimental tensile stress T and strain into the Fung model yields G_{inft} = 7.01 kPa and b = 0.17 with R^2 = 98.9 %. The normalized

MRE shear storage modulus appears to increase by the amount of uniaxial pre-tension load inflicted on the specimen for deformation states of up to 80% strain.

TABLE III
MRE SHEAR STORAGE MODULUS AND TENSILE STRESS FOR ALL STRAINS

ε (%)	$G_{1.5}$ (kPa)	$G_{2.0}$ (kPa)	$G_{2.5}$ (kPa)	G_0 (kPa)	T (kPa)	Grip
0	70.84	75.55	80.77	55.86	0	small
20	67.03	73.2	78.85	49.39	1.8	small
40	73.39	78.01	83.44	58.18	5.3	small
60	84.09	88.95	95.58	66.56	11.4	medium
80	84.48	91.11	95.6	68.16	13.2	medium
100	90.9	97.67	96.98	83.02	17.6	big
120	87.31	105.32	91.84	85.76	22.8	big
140	36.28*	105.71	93.06	-35.21*	29	big

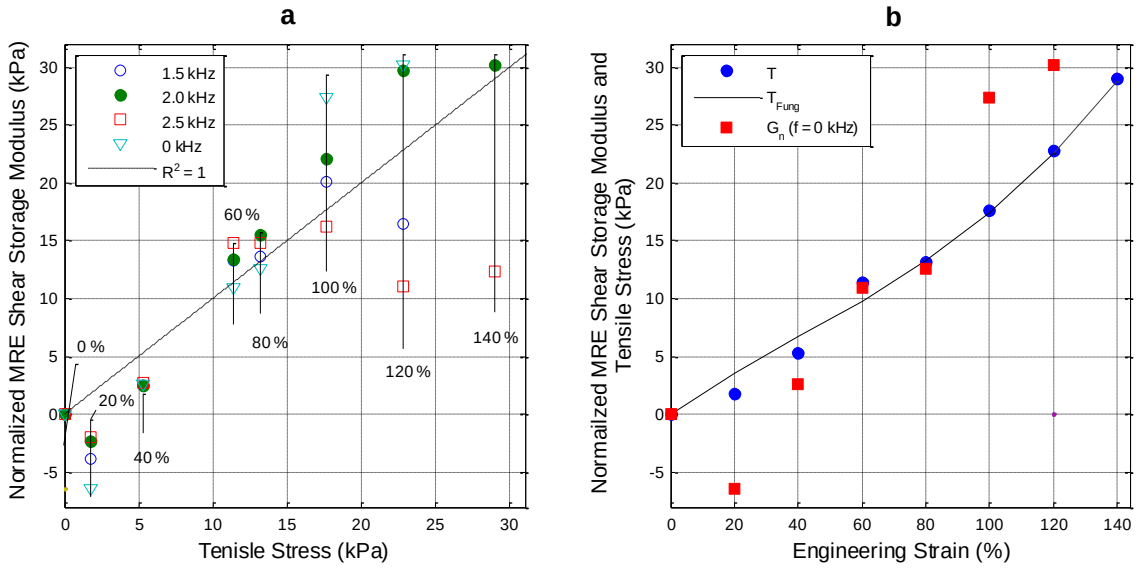

Figure 6-9: (a) Comparison between tensile stress and G_n. (b) Experimental tensile stress, Fung hyperelastic model tensile stress, and normalized storage shear modulus at f_e = 0 kHz plotted with strain. T: Experimental tensile stress from. T_{Fung}: Fung model tensile stress from (2.25) with G_{inft} = 7.01 kPa and b = 0.17 with R^2 = 98.9 %. G_n: $G_n(f = 0$ kHz).

TABLE IV
TENSILE STRESS AND SHEAR STORAGE MODULUS CORRELATION

Frequency (kHz)	Spearman's rho	p-value
0	96.4 %	0.003
1.5	92.9 %	0.007
2	97.6 %	< 0.001
2.5	61.9 %	0.115

6.4 Discussion

Currently, there are no commercially available tensile testing systems that are MRI compatible and include an MRE actuation mechanism. To our knowledge, the presented work represents the first published information on how to design and build such a system, which was entirely custom-built with MRI compatible materials. The design addresses the challenges of simultaneously introducing a specimen with vibrations and pre-tension while in a small-bore MRI system. Particularly, the spatial design constraints of the AGM were difficult to overcome since the radial distance between the specimen surface and RF coil inner diameter is 0.68 cm. The novelty is the AGM's functional ability to keep constant grip contact pressure around the specimen as its diameter changes from elongation in such a small space. Another design constraint is related to pre-tension in that the specimen had to be elongated 17.8 cm beyond its undeformed state (to achieve 140 % strain) via a pulling string but yet, not disrupt the mechanisms responsible for vibration, gripping, AGM positioning, and centering the specimen in the magnet. As described in Section 3.2, all the components of the Tensile-MRE probe were required to function in coordination with experimental timeline of the tensile test and MRE data acquisitions. Therefore, the probe design in this study may be valuable to the development of apparatuses used in future MRI investigations related to mechanical behavior of materials in tension or high frequency vibration.

Improvements for future systems should also include refinements to the actuation system. Small specimen sizes require high excitation frequencies during MRE to create an adequate number of wavelengths for inversion based data processing. Piezoelectrics seem to be the only MRI compatible actuators available for frequencies above 1,000 Hz. However, piezoelectric stacks are very sensitive to overbearing bending, torque, and tension stresses. Several stacks were damaged during developmental testing of the Tensile-MRE probe. More studies need to focus on designing robust piezoelectric systems that can handle resilient interaction with specimens during dynamic material testing.

Soft biological tissue and synthetic elastomer moduli obtained from tensile testing are dependent on strain rate as seen in Young's modulus of excised pig brain and Ecoflex (Rashid *et al* 2014, Franculli 2013). The MRE scan time (approximately 7 minutes) required for one frequency and one strain increment limits the timing of the force measurements in the tensile test. In the presented work, tensile force and MRE data were acquired only when the specimen remained in static states of tensile deformation (held still at each strain increment). Therefore, strain rate was not considered as a factor in this demonstration study.

To identify possible influences of specimen relaxation, a pretest conducted prior to the main Tensile-MRE experiment included hanging the load cell, specimen, and a 1.13 Kg weight in series. From the moment the total vertical tensile force of the weight was loaded onto the specimen, there were no observable changes in the tensile force measurement for 10 minutes. Therefore, it is assumed material relaxation after each increment of specimen elongation did not impact the tensile force measurements.

In one MRE validation study, a compression test used a hyperelastic model to calculate infinitesimal shear modulus and found the MRE derived shear stiffness to be close in value (Leclerc et al. 2012). However, the relationship and dependencies of the compression test strain rate and MRE excitation frequency are not mentioned as a factor in the study. MRE was also compared to dynamic shear testing where the dynamic shear frequency was matched with MRE excitation frequency (Ringleb et al. 2005).

The study found a good correlation between the two methods. Yet, the shear moduli from the dynamic shear test changed with compressive clamping strain. This is in line with our observations that the MRE shear storage modulus increases with rising actuator grip pressure as shown in Figure 6-5(a). In a pretest we used a threaded rod for the AGM to close the gap between the grip collars but we were unable to keep a constant torque on the threaded rod. The grip contact pressure could not be kept consistent through all strain increments and MRE scans using the threaded rod but this could be achieved via plastic syringes. Grip contact pressure consistency during MRE actuation was imperative to distinguish that shear storage modulus changes were resulting from tensile elongation and not from changing experimental conditions. Consistent grip contact pressure and actuator contact for transmitting vibrations into specimens should be carefully assessed in future studies where MRE is compared to other material testing methods.

MRE has been applied to specimens undergoing pre-tension before using other actuation methods. In one study, a Wirosil gel phantom (2.5 x 2.5 cm square bar x 16 cm long) was placed lengthwise over two supports and loaded to tensile stresses of 0, 35, 70, and 105 kPa while an electromechanical driver was placed halfway between the supports and delivered vibrations in the frequency range of 100 to 450 Hz. The actuation was delivered on one side lateral to the phantom length while the tension was induced by tethering the specimen ends to free hanging weights on a pulley system. Wavelength measured by MRE increased with tensile loading (Chen et al. 2006), which is in agreement with our observations (Figure 6-7(a & c) because higher values of the shear storage moduli involve longer wavelengths.

In our experiments we did not observe any correlation of the longitudinal modulus, L from (2.12) with the state of tensile deformation. The 1st Lame-parameter is mostly related to compression waves that were filtered using the Butterworth bandpass filter during processing of the MRE data. Comparing the two processing approaches for the complex shear moduli G^* (2D) and G (3D), the 3D modulus shows a monotonic relation with the strain and was therefore used for correlation analysis with the experimental tensile stress T. The observed relationship of MRE stiffness and pre-tension may be important to other

studies such as voluntary muscle MRE. When investigating muscle stiffness in relation to loading, it may be important to investigate muscle stiffening induced by passive tensile reaction stress (loading induced by elongation). Most of the voluntary muscle MRE studies only consider stiffening from muscle fiber activation. The direction of pre-tension is noticeable in the MRE shear storage moduli where G and g_z show the same trend (Figure 6-8(a)). This may be valuable information for directional stress analysis in future applications.

The incremental stretching behavior of the Ecoflex fits the Fung model well with $R^2 = 0.989$. Thus, using hyperelastic models at large strains (140 %) is a promising avenue for studying viscoelastic material responses to pre-tension. Although the Fung model infinitesimal shear modulus G_{inft} of 7.01 kPa does not match the MRE shear storage modulus G (f = 0 Hz, $\varepsilon = 0$ %) of 55.86 kPa, the tensile stress T has a strong strain dependent correlation with the shear modulus G_n at most frequencies (Table IV).

MRE-derived stiffness measures are sensitive to experimental conditions and parameters such as signal to noise ratio, mechanical excitation frequency, spatial resolution, and data filtering. Ideally to improve MRE reliability, there should be a community standard developed, which includes a systematic testing method to measure the stiffness of a reference phantom (using MRE and a partner measuring method for stiffness comparison) and a parameter optimization scheme for the calibration of post processing software based on the reference phantom stiffness. There are two concepts learned from conducting the Tensile-MRE experiment that can be incorporated into future standard protocols for calibrating MRE systems. 1) Shear storage modulus seems to increase by the magnitude of uniaxial tensile load inflicted on the specimen as seen in Figure 6-9(b). Therefore, the proposed method may be used to span a range of stiffness values using only one MRE reference phantom by mimicking increases in shear stiffness through strategic pre-loading. Tuning MRE systems for a range of stiffness values will increase MRE measurement quality. 2) Many benefits would come alongside conducting an MRE reference material test simultaneous with a partner measuring method. Reference phantom preparations, temperature effects, and shelf life time regarding phantom stiffening could be disregarded when

performing the MRE calibration using a standard reference phantom and partner method at the same time. Calibration accuracy and reliability would depend on the phantom shear modulus value found with force and strain gauges of the partner method and be used to optimize the corresponding MRE derived stiffness. The quality of the concurrent measurement calibration strategy would not be influenced by the reliability of the reference phantom to keep consistent mechanical properties.

This study demonstrated MRI-compatible tensile testing during MRE, from which a novel Tensile-MRE experimental platform was developed. The results revealed a pre-tension and stiffness correlation (through 3 frequencies up to ≈ 80 % strain) that could lead to new calibration techniques using a predetermined tensile loading mechanism.

Acknowledgments

The authors thank Steve Kearney of the University of Illinois at Chicago for his pulse sequence development help. And also Eric Schmidt, David Mecha, Thomas Bruzan, and Matthew Schuck of Research Resources Center of the University of Illinois at Chicago for their input on machining methods.

TABLE V
MATERIALS USED IN TENSILE-MRE PROBE

Material	Dimensions or Type	Function	Supplier
Aluminum s-type force transducer	100 N, model: 661.09B-21	tensile force measurement	MTS Systems Corp
Aluminum round bar	Various	piezoelectric housing ends	McMaster-Carr
Brass screws	2-56"	connecting actuator components	McMaster-Carr
Copper tube	1-1/2" OD, 1-15/16" ID	connecting housing to slide rail	McMaster-Carr
Delrin round bar	various	grips and grip collars	McMaster-Carr
Flame-retardant garolite (G-10/FR4)	1/16"	transfer syringe movement to grips	McMaster-Carr
Hard & strong garolite (XX)	1-5/16" OD, 1-1/4" ID	actuator sleeve	McMaster-Carr
Heat shrink tubing	1/16", 3/32"	lock garolite rods in actuator	TE Connectivity
Polycarbonate round tube	1-1/2" OD, 1-3/8" ID	probe housing	McMaster-Carr
Nylon plastic screws	2-56"	connecting actuator components	McMaster-Carr
Piezoelectrics	P-840.10	mechanical actuation	Physik Instrumente L.P.
Plastic syringe	3 ml	compress grip collars	BD Medical
PVC round bar	various	plastic rings for pulling specimen	McMaster-Carr
Rubber bands	1/32" thick	expand grips during grip release	Alliance Rubber Co

CHAPTER 7

RELATING DYNAMIC SURFACE AND INTERNAL DISPLACEMENT FIELDS IN SOFT TISSUE-MIMICKING MEDIA: SYNCHRONOUS ACQUISITION OF MRE AND SLDV

7.1 Introduction

New avenues of experimental platforms for probing mechanical surface and interior wave propagation in viscoelastic media with noninvasive imaging techniques are important to further the development and measurement quality of soft tissue elastography. These types of investigations are appropriate especially as elastography continues to become more accessible as a clinical diagnostic tool. The primary aim of this study is to combine the scanning capabilities of SLDV and MRI to collect displacement measurements on the surface and inside, respectively of a viscoelastic homogeneous media undergoing mono-frequency steady state mechanical excitation. Technical challenges were overcome to enable the two imaging modalities to operate within the limitations of a high magnetic field environment and synchronously acquire data from the same specimen. The investigation provides valuable insight to further understand wave propagation in biomedical applications in relation to mechanical properties.

Several studies have been conducted on surface wave elastography using SLDV for investigating human tissue for voluntary muscle, skin, eye, facial muscle, and respiratory characteristics of lung (Salman & Sabra 2013; Kearney et al. 2015; Altaf A. Khan et al. 2013; Tabatabai et al. 2013; Peng et al. 2014). All results from OE yield shear moduli calculated from surface waves acquired from SLDV to analyze the mechanical characteristics of the soft tissue regions. A large number of MRE studies have also investigated tissue stiffness using MRI such as brain, liver, lung, voluntary muscle, heart, breast, kidney, and spleen using internal displacement fields (Yogesh K Mariappan, Kevin J Glaser 2011). In most MRE analysis, inversion techniques are used to determine shear modulus from tissue internal displacement fields acquired using MRI phase data.

The combination of SLDV and MRI has not yet been acquired concurrently in the same platform to collect displacements directly from the specimen, however SLDV has been used in MRE investigations to gauge the displacement amplitude of mechanical drivers. Rigid bar and passive drum drivers, being the most common MRE actuation designs, have been evaluated with SLDV for experimental design evaluation before use in MRI systems (Arani et al. 2011; Leclerc et al. 2012). In some studies laser position is reflected from a mirror attached to actuators to measure actuator displacements during MRE data acquisition (Muthupillai et al. 1995; Uwe Hamhaber, Uwe Klose, Frieder Grieshaber 2001) .

The relationship between surface and internal displacement fields has been explored through computer simulation. A simulation of a vibrating ball with a cylindrical elastic media was analytically solved to better understand the boundary conditions of different oscillating geometries that mimic shear wave propagation through organs (Schwartz et al. 2016). Experimentally derived mechanical coefficients acquired from surface measurements have been used as boundary conditions to model surface displacement relationships to internal organ function. SLDV was used to measure displacement fields on the backs of humans while a rigid driver introduced steady state vibrations to the chest. The experimental surface displacement fields correlated well to the simulation fields derived from analytical solutions of sound transmission through human chest to back (Royston et al. 2011).

MRE is not the only MRI method capable of acquiring dynamic displacement field measurements. Vibration-synchronized MRI characterizes tissue mechanics using MRI synchronized with vibration strain and not with motion encoding gradients as used in MRE pulse sequencing (Elgeti et al. 2012). Excitation frequencies above 80 Hz experience more attenuation as vibrations penetrate further into internal human tissue from the external source. Hence, acquiring displacement fields equivalent to strain images at lower frequency vibrations involves less internal dampening.

7.2 Materials and Methods

7.2.1 Specimens and Actuation System

Ecoflex and Plastisol are used as the specimens and are subjected to identical experiments. Specimens were poured and solidified into acrylic 13.97 and 5.72 cm outside diameter cylinders both with 0.3 cm wall thickness and 7.62 cm in length. All cylinders were left open on either side after curing exposing the flat ends of all specimen surfaces (Figure 7-1(A)). The exposed front ends of the specimen surfaces were coated with reflective microbeads to enhance laser reflection quality. The microbeads have a refractive index greater than 1.93 and size = 35 to 45 microns (Cole Safety Products, USA). The specimen cylinders are press fit to an acrylic actuation disk that is mounted to a piezoelectric stack during experiments (Model P-840.10, Physik Instrumente GmbH & Co, Germany) within the actuation system. Several holes were cut into the actuation disk to avoid pressure build up between the disk and specimen from changing volume during actuation. An airtight seal results in inducing pre-stress on the specimen, which was found to increase surface wave attenuation in the specimen during the preliminary testing of the actuation system development. A large cylinder specimen is seen connected to the actuation system in Figure 7-1(B). Three small cylinder specimens at a time where placed on the same actuation disk during data acquisition. The entire actuation system was placed into a 150 mm diameter RF birdcage coil (RAPID Biomedical GmbH, Germany) within a 9.4 T MRI magnet (Model 310 mm Bore Actively Screened Magnet System, Agilent Technologies, Research Products, USA) for all experiments. The specimen cylinders slide freely as the piezoelectric oscillates. A thick walled 0.8 cm diameter rubber tube wraps around the actuation system hub that is manually expanded to rigidly ground the hub to the magnet bore and can be loosened for specimen repositioning. The entire action system was machined out of plastic other than the piezoelectric actuator.

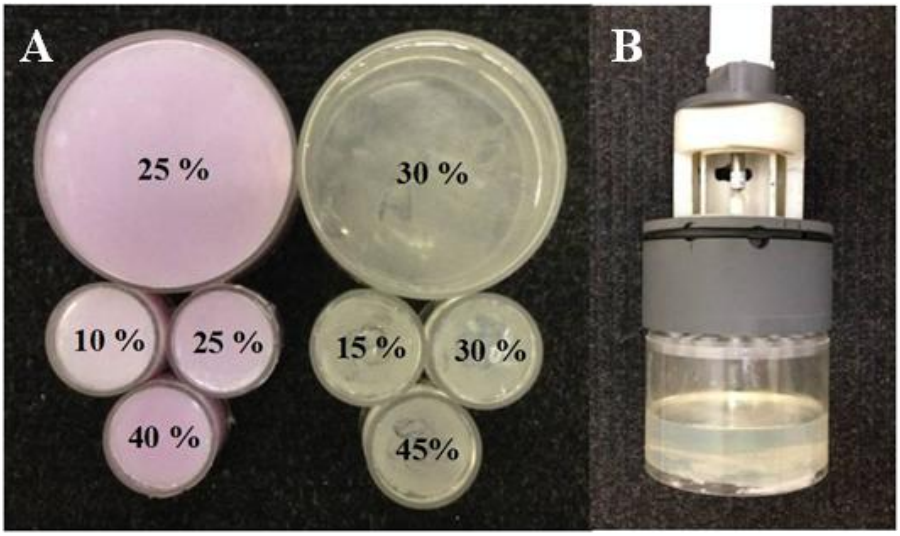

Figure 7-1: (A) Cylindrical specimens used in experiments (Ecoflex and Plastisol to the left and right, respectively). Numbers indicate softener concentration percentage. (B) Actuation system with piezoelectric connected to actuation disk pressed onto the large diameter Plastisol specimen.

7.2.2 Experimental Platform and Data Acquisition

Figure 7-2 illustrates the specimen connected to the actuation system position in the magnet center while SLDV (Model PSV-400 Scanning Vibrometry, Polytec GmbH, Germany) measures surface displacements and MRE obtains internal displacements from the vibrating specimen. The SLDV system had to be positioned outside of the magnet room (operation had to occur outside the fringe fields of the magnet) where it was pointed towards a surface first mirror (0.485” thick glass sheet x 11" x 13" inches, Kaleidoscopes To You, USA) located in front of the magnet (Figure 7-3(A)). The mirror was used to redirect the SLDV optical view and laser at a right angle down the magnet bore onto the specimen front surface (Figure 7-3(B)). Figure 7-8 at the end of Chapter 7, shows a picture of the SLDV system positioned in the MRI suite during synchronous MRE and SLDV experiments.

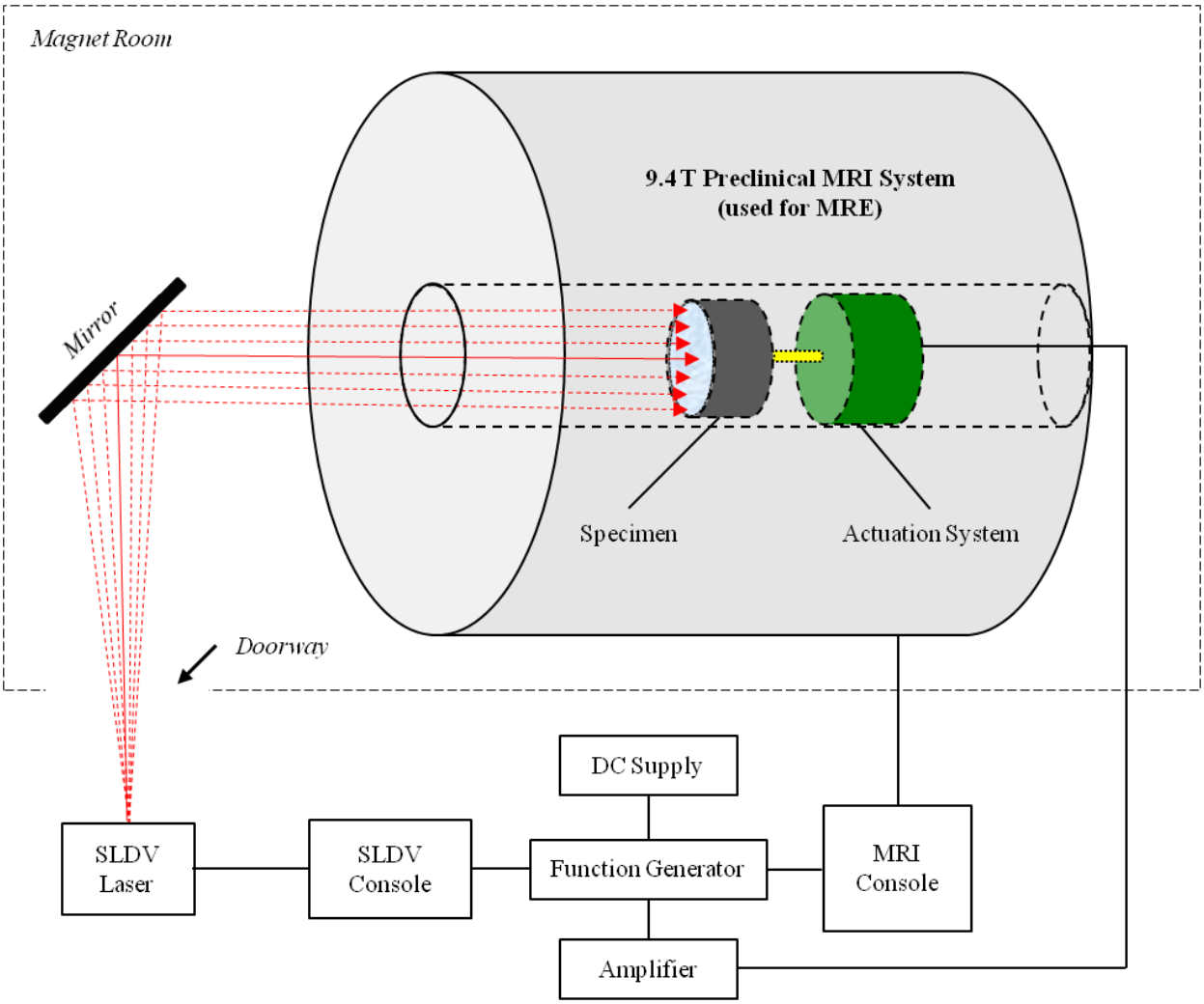

Figure 7-2: Schematic representing the experimental platform used for synchronous acquisition of SLDV and MRE of a large diameter cylindrical specimen.

Plastisol and Ecoflex were both used in the same scanning protocol. The piezoelectric was controlled and powered by a function generator connected in series with a variable audio amplifier and DC power supply. An output trigger was linked from the MRI console to the function generator and an output reference was connected from the function generator to the SLDV console. These communications were necessary to keep the mono-frequency and steady sate mechanical excitation cycling of the piezoelectric in synchronization with the MRI and SLDV data acquisitions. The SLDV system acquired surface displacements perpendicular to the radial dimension of the specimens established by 8 lines of 79

spatial data points in a polar array distributed evenly over the specimen front surface (Figure 3(C)). Every data point was recorded 3 times and averaged. The timing of all spatial data points was acquired relative to phase = 0. The large specimens were scanned separately, whereas the small specimens of the same material were scanned 3 at a time.

Figure 7-3: (A) First-surface mirror used in experiments. (B) Large cylinder specimen in center of magnet. (C) Polar grid of SLDV data points seen through SLDV user interface overlaid onto specimen front surface.

A SLIM MRE pulse sequence was used to acquire z, x, y direction internal displacements at the same time (z-direction is perpendicular to the axial image plane). The scan parameters are TR = 1,615 ms, TE = 72.67 ms, matrix = 96 x 96 (large specimens) or 128 x 128 (small specimens), FOV = 16 x 16 cm, slices = 8, thickness = 0.4 cm, slice plane = axial, number of motion encoding gradients = 2 or 4, gradient strength = 8 G/cm, phase offsets = 8. The piezoelectric was powered with approximately 100 volts peak-to-peak and continuously oscillated sinusoidal at the excitation frequency throughout the entire scan. The large specimens were scanned at 60, 100, 150 Hz and the small specimens at 250 Hz. Each scan was repeated 3 times. Immediately after the MRI data acquisition began, the SLDV data acquisition was manually started. The MRI scan time was approximately 40 minutes with the total SLDV acquisition taking less time. A total of 36 coupled MRI-SLDV scans were conducted in the study with variations in

excitation frequency, specimen stiffness, and material type. The complex shear moduli G_1 and G_{su} calculations are shown in Chapter 2 for MRE and OE, respectively.

7.3 Results and Discussion

7.3.1 Displacement Fields

The displacement fields for MRE and the corresponding SLDV measurements of the large Ecoflex specimen undergoing 60, 100, 150 Hz mechanical excitation and the small Ecoflex specimens of different stiffness at 250 Hz are shown in Figure 7-4 and Figure 7-5, respectively representing material displacement perpendicular to the radial dimension of the specimens. Wave images were constructed by visually matching the phase of the MRE to the SLDV. The images presented are from the first trials of each frequency data set. SLDV is spatially collected from the surface in an 8-line polar array with 79 points per line. MRE is collected in a 96 x 96 matrix Cartesian grid with 1.67 x 1.67 mm pixel size from the 4 mm thick slice closest to the surface. The distinct difference between the measurements is that the SLDV is recorded with changes in reflected laser frequency response due to oscillating surface displacements and the MRE is obtained from the accumulation of proton magnetic spins within the 4 mm slice material media representing the fluctuating internal displacement fields. Material response to oscillating mechanical excitation is visually similar in the form of shear wave motion for both MRE and SLDV found within their dynamic displacement fields.

However, the displacement field analysis is limited to a visual qualitative comparison since there is some ambiguity in the data collection approach of SLDV in relation to the MRE regarding space and time. Spatially, the alignment of the coordinate systems was verified by line-of-sight through the overlay of the polar grid onto the front surface of the specimen through the SLDV camera FOV and from the specimen position within the MRI coordinate matrix. The visual positioning and angles of the mirror and SLDV laser scanning head may be partially responsible for the position offsets in Figure 7-4 and Figure

7-5 between MRE and SLDV in the displacement profiles. The center offset correction factor, X_3 in the SLDV curve-fitting algorithm partially compensates for positioning errors. Temporally, zero phase of the MRE data acquisition was not matched to that of the SLDV measurements. Although phase = zero for both MRE and SLDV were referenced to the starting phase of piezoelectric oscillations, the SLDV was manually initiated approximately 10 seconds after the MRI data began recording. Therefore, the phase offset between the MRE and SLDV cycles were estimated by visualization in order to sync together the images between the two modalities in Figure 7-4 and Figure 7-5. An SLDV scan took approximately 1/3 the time of its corresponding MRI scan.

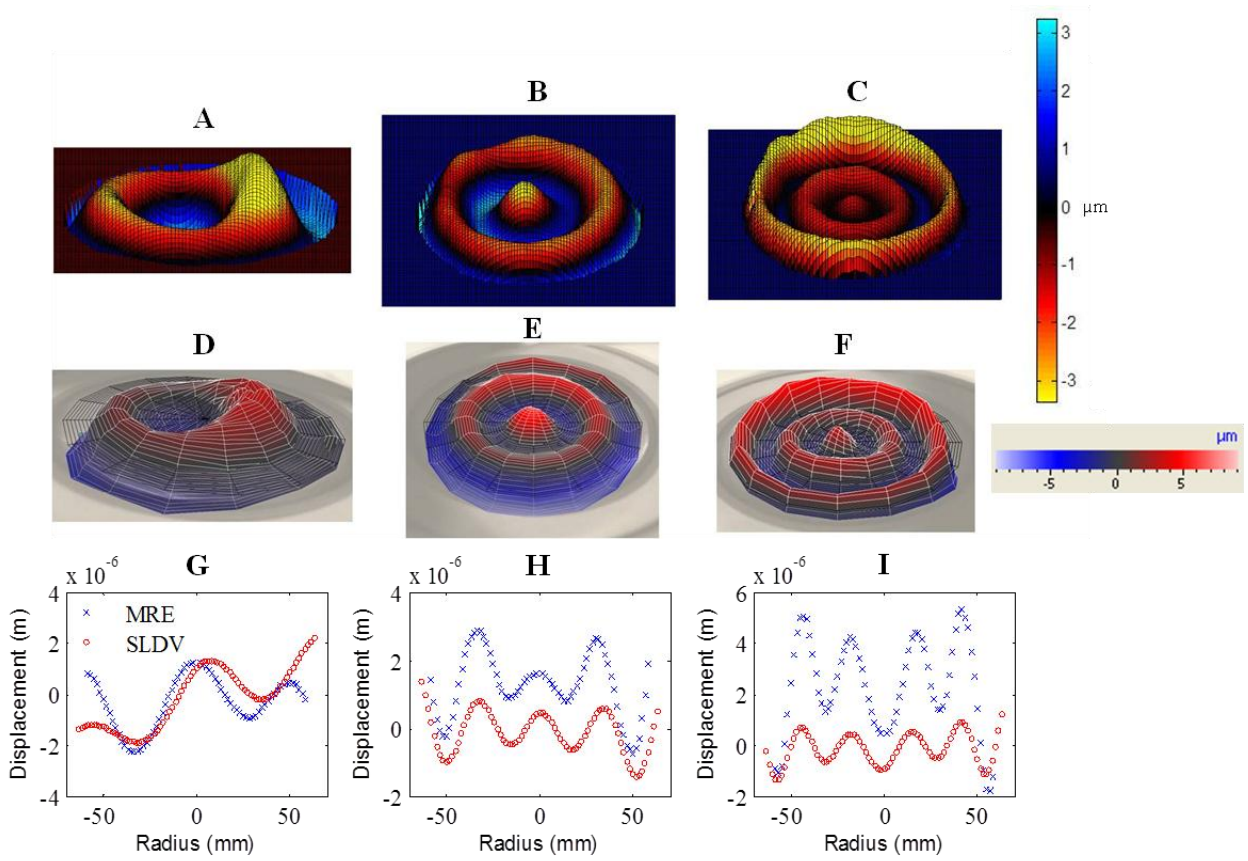

Figure 7-4: Comparison between surface and internal displacement fields for the large Ecoflex specimen with increasing frequency acquired by SLDV and MRE, respectively (perpendicular to specimen axial plane). Data was collected synchronously between both imaging modalities for each individual excitation frequency. (A) 60, (B) 100, (C) 150 Hz for MRE. MRE wave motion images are from the axial slice of 4 mm thickness closest to specimen front surface. (D) 60, (E) 100, (F) 150 Hz for SLDV. SLDV wave images are acquired from the specimen front surface. (G) 60 Hz, (H) 100 Hz, (I) 150 Hz of a 1D displacement profile using a horizontal line across the entire specimen diameter passing though its center. Images in the top two rows are isometric surface plots of the axial plane displacement fields.

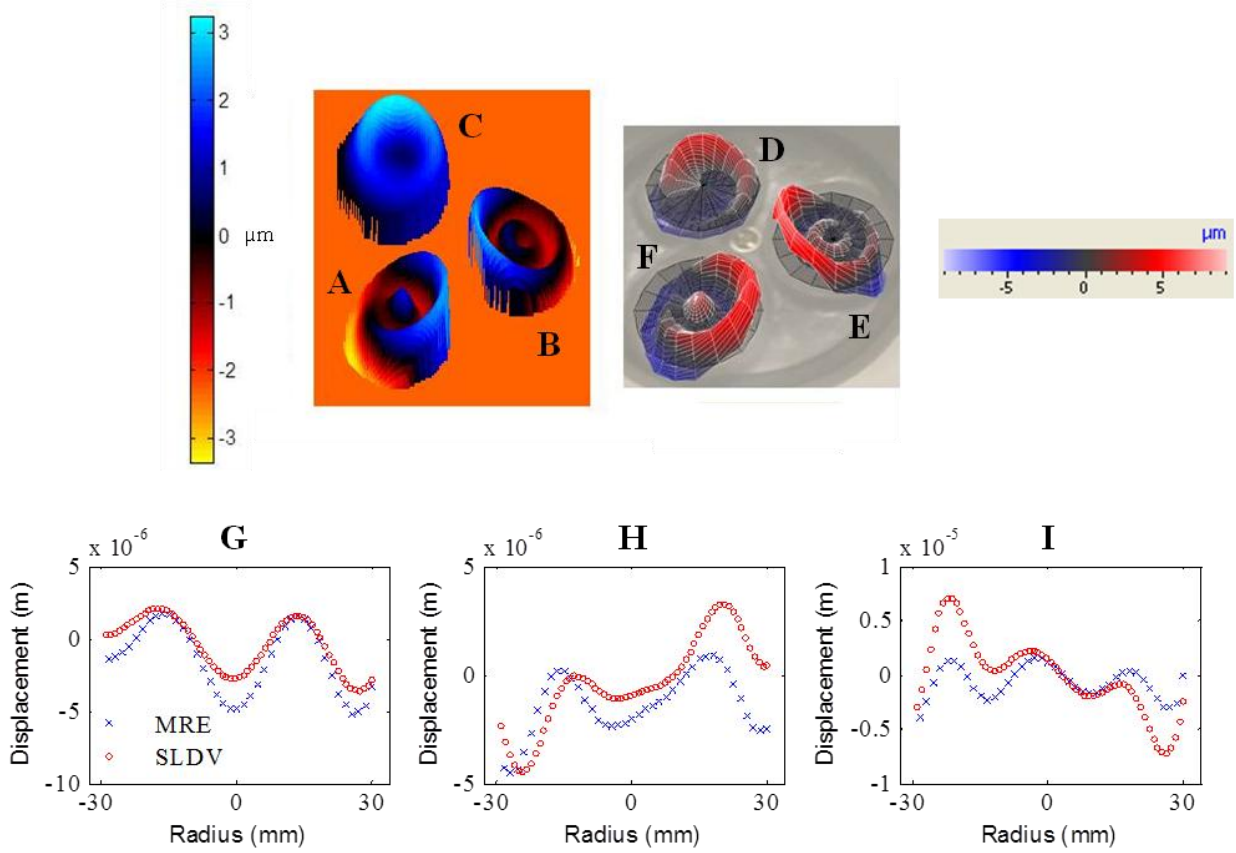

Figure 7-5: Comparison between surface and internal displacement fields for the small Ecoflex specimens with increasing specimen stiffness at 250 Hz acquired by SLDV and MRE, respectively (perpendicular to specimen axial plane). (A) 40, (B) 25, (C) 10 % softener concentration for MRE. (D) 40, (E) 25, (F) 10 % softener concentration for SLDV. (G) 40, (H) 25, and (I) 10 % softener concentration of a 1D displacement profile using a horizontal line across each specimen diameter passing though its center. Images in the top two rows are isosurface plots of the axial plane displacement fields.

7.3.2 Elastography Comparison

MRE and OE derived complex shear moduli (3 samples per data point) are shown in Figure 7-6 for Plastisol and Ecoflex for 60, 100, 150, 250 Hz and for different specimen stiffness. G' and G" are the storage (real part) and loss (imaginary part) shear modulus, respectively. Numerical values of Figure 7-6 are listed in TABLE VI. Storage and loss shear modulus increases with frequency for MRE and OE. The increases were expected since shear wavelength increases with excitation frequency for a given material. Each SLDV storage modulus at 60 Hz is considerably higher than MRE moduli at 60 Hz since there were

not enough wavelengths propagating over the large specimen surface at 60 Hz. Using the 'Levenberg-Marquardt' curve-fitting algorithm to acquire wavenumber for calculating OE complex shear modulus becomes inaccurate when there is a small number of wavelengths present in the 1D profile being assessed. The predetermined stiffness of the large specimens were chosen to reflect storage shear modulus values of human soft tissue measured with MRE, which use excitation frequencies between 60 to 150 Hz (Yogesh K Mariappan, Kevin J Glaser 2011). MRE storage shear modulus was 1.65 ± 0.25 kPa for Plastisol (30 % softener) and 7.52 ± 1.10 kPa for Ecoflex (25 % softener) at 60 Hz for the large specimens and are in range of human soft tissue stiffness.

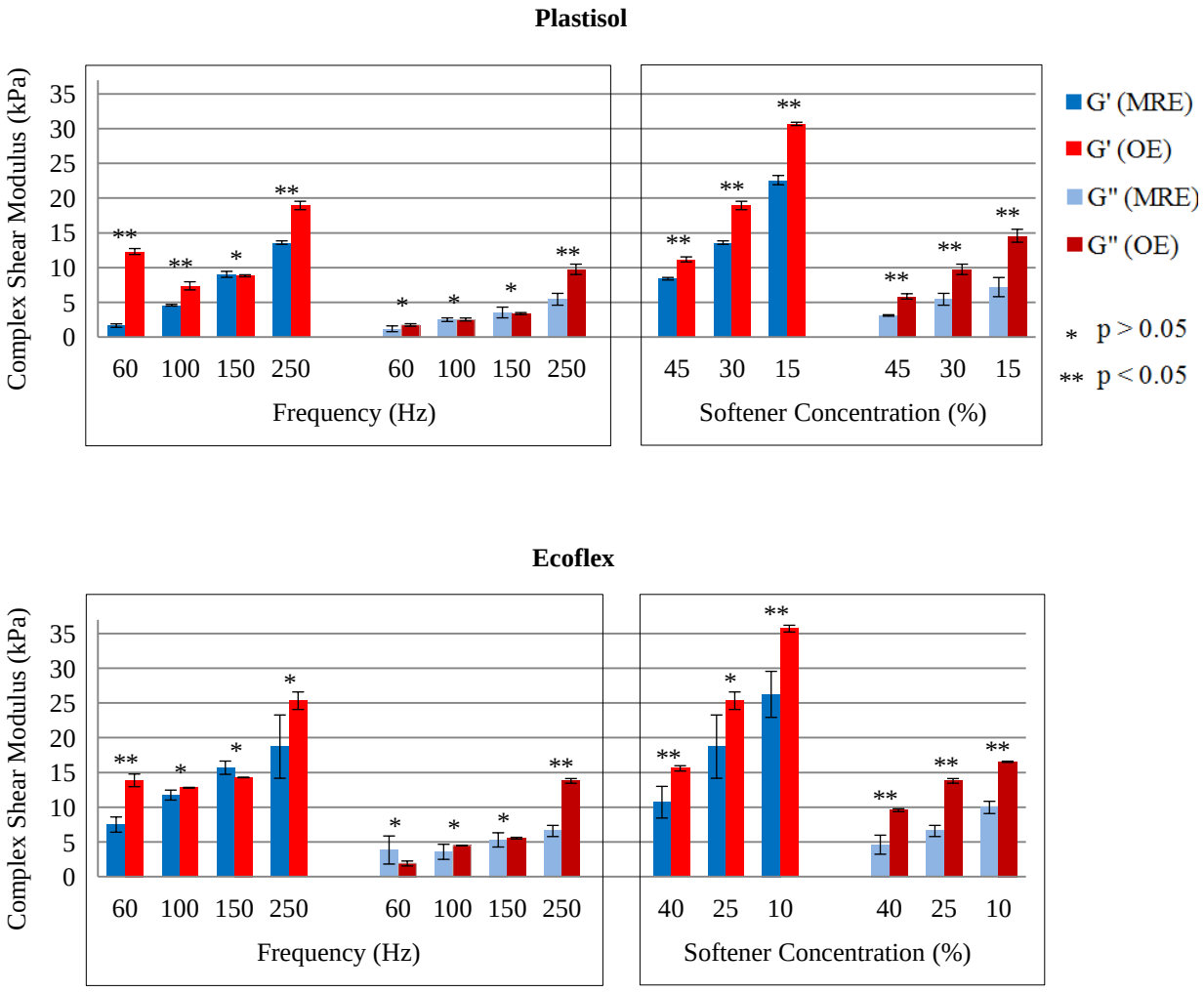

Figure 7-6: MRE and OE values for complex shear modulus for increasing frequency and specimen stiffness with Plastisol and Ecoflex. The p value represents a student t-test between MRE and OE moduli for each varying frequency and stiffness scenario with $p > 0.05$ meaning the values in the comparison are not significantly. Error bars represent standard deviation with 3 samples per data point. Real and imaginary parts of the complex shear modulus are at the right and left sections of the individual bar graphs, respectively.

TABLE VI
COMPLEX SHEAR MODULUS COMPARISON BETWEEN MRE AND OE

		G' (kPa)		G'' (kPa)	
Type	**Frequency (Hz)**	**MRE**	**SLDV**	**MRE**	**SLDV**
Plastisol (30 % softener)	60	*****1.65 ± 0.25	12.32 ± 0.43	1.19 ± 0.42	1.75 ± 0.18
	100	4.58 ± 0.12	7.73 ± 0.59	2.5 ± 0.26	2.54 ± 0.21
	150	9.03 ± 0.43	8.82 ± 0.15	3.54 ± 0.77	3.38 ± 0.14
	250	13.6 ± 0.25	18.94 ± 0.61	5.44 ± 0.85	9.75 ± 0.75
Ecoflex (25 % softener)	60	7.52 ± 1.1	13.89 ± 0.91	3.86 ± 2.02	1.92 ± 0.35
	100	11.76 ± 0.72	12.83 ± 0.05	3.6 ± 1.08	4.51 ± 0.13
	150	15.71 ± 0.95	14.3 ± 0.03	5.31 ± 1.02	5.56 ± 0.13
	250	18.74 ± 4.55	25.35 ± 1.26	6.6 ± 0.8	13.81 ± 0.34

		G' (kPa)		G'' (kPa)	
Type	**Softener (%)**	**MRE**	**SLDV**	**MRE**	**SLDV**
Plastisol (250 Hz)	45	8.4 ± 0.18	11.18 ± 0.37	3.11 ± 0.11	5.84 ± 0.38
	30	13.6 ± 0.25	18.94 ± 0.61	5.44 ± 0.85	9.75 ± 0.75
	15	22.59 ± 0.67	30.69 ± 0.24	7.19 ± 1.38	14.59 ± 0.93
Ecoflex (250 Hz)	40	10.74 ± 2.28	15.61 ± 0.38	4.62 ± 1.37	9.6 ± 0.2
	25	18.74 ± 4.55	25.35 ± 1.26	6.6 ± 0.8	13.81 ± 0.34
	10	26.27 ± 3.31	35.73 ± 0.49	9.99 ± 0.88	16.56 ± 0.09

*** Mean ± SD, u = 3**

Storage and loss modulus also increased with specimen softener concentration decrease (Figure 7-6). The softener concentration was linearly decreased for the 3 small specimens to mimic multiple regions of different stiffness to access measurement of stiffness variation in the same scan. Several MRE studies have investigated specimen stiffness variation embedded in a surrounding soft material media where the excitation vibrations were introduced at the exterior of the embedded material while the shear wave propagation continued through to the varied stiffness ROIs (Yin et al. 2014). Here, each varied stiffness region was placed in its own individual rigid cylinder for excitation by geometric focusing. Although it is important to study MRE derived stiffness of inhomogeneous and anisotropic media, this setup was constructed in order to avoid interferences in wave propagation from neighboring areas of different stiffness for obtaining more accurate measurements.

In this work, OE moduli tend to be greater than MRE moduli. MRE shear modulus is derived using inverse methods where 2-3 numerical derivatives need to be applied to noisy data in order obtain the shear modulus. This tends to amplify the noise, and in turn artificially creates very short wavelengths in the data. Short wavelengths are related to soft material lowers the average MRE shear modulus compared to OE. Also, since MRE inversion included x, y, and z direction displacements, whereas OE only involved the z direction of displacement, this factors could impact the differences in complex shear moduli between the two elastography methods. Student's t-test was performed for each comparison between MRE and OE modulus (Figure 7-6). The excitation frequency of 150 Hz for all materials is not statically different ($p > 0.05$) for both storage and loss shear moduli. This is most likely because the frequency had an adequate number of wavelengths propagating through the 13.97 cm diameter specimen at 150 Hz compared to all other frequencies and corresponding specimen sizes that yields more precise measurements. The entire study included 36 coupled sets of simultaneous MRI and SLDV acquisitions corresponding to MRE and OE complex shear moduli. The storage and loss modulus for each MRE and OE set related by synchronized order of acquisition is plotted in Figure 7-7 that yields a Pearson's correlation of rho = 0.88 with $p < 0.001$ for storage modulus and $\rho = 0.85$ with $p < 0.001$ for G" loss modulus.

The simultaneous comparison of MRE and OE in this experimental platform exhibits advantages compared to other MRE validation studies. Oscillatory rheometry, dynamic shear testing, and compression, which have been used to validate MRE derived shear modulus, do not have the ability to visualize shear wave propagation (Klatt, Friedrich, et al. 2010; Clayton et al. 2010; Hamhaber et al. 2003). Although these studies provide contrast to other classes of material testing that yield shear modulus, they derive moduli values from strain and forces gauges, whereas elastography uses image based measurements of mechanical wavelength. Ultrasound elastography however, is similar to MRE but uses a transient compression wave source (MHz range) to create shear wave motion in a particular ROI where an ultrasonic imaging probe collects material wavelength data for shear moduli analysis (Zsch

2015; Xie et al. 2012). Optical imaging elastography methods are more similar to MRE in that they typically excite vibrations with mechanical drivers at steady state and mono frequencies (Kearney et al. 2015).

Geometric focusing excitation was chosen in the experiments since the resulting surface and internal wave motion would primarily oscillate symmetrically over the axial plane of the specimen. Casting the material into cylinders and using geometric focusing eliminates the need to physically grip specimens during actuation. Pre-stresses from gripping the specimens during mechanical testing influences yielding shear moduli as observed in other MRE validation studies were the validation method required loading interaction with strain and force gauges (Ringleb et al. 2005; Oudry, Vappou, et al. 2009). No elastography study has examined wave propagation from one excitation source with two separate imaging modalities at the same time.

Synchronous MRE and OE measurements from the same vibration source were collected to study the mechanical properties of a synthetic viscoelastic material. A novel experimental platform for synchronous SLDV and MRE data acquisition was developed to achieve concurrent MRE and OE comparison. The results indicate that SLDV and MRE are precise methods of measuring soft tissue-mimicking material displacements during mechanical excitation.

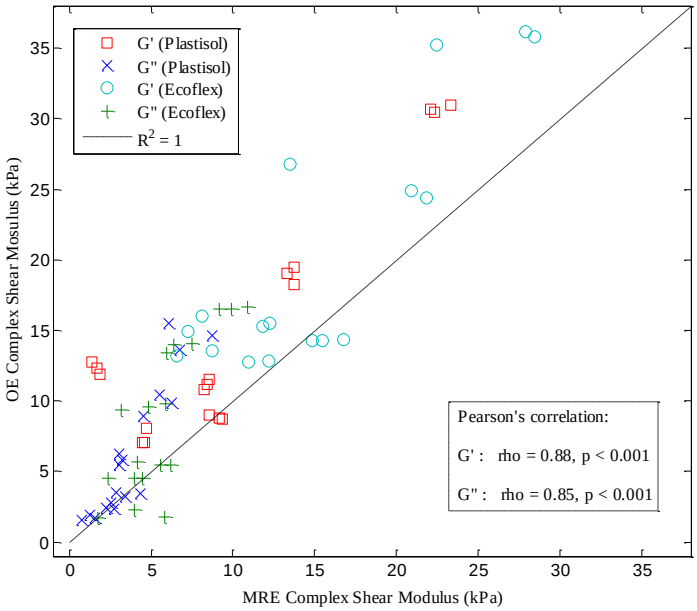

Figure 7-7: Correlation between MRE and OE complex shear moduli related by coupled scan. Data points include all 36 sets of scans obtained in study for variations in frequency, stiffness, and material.

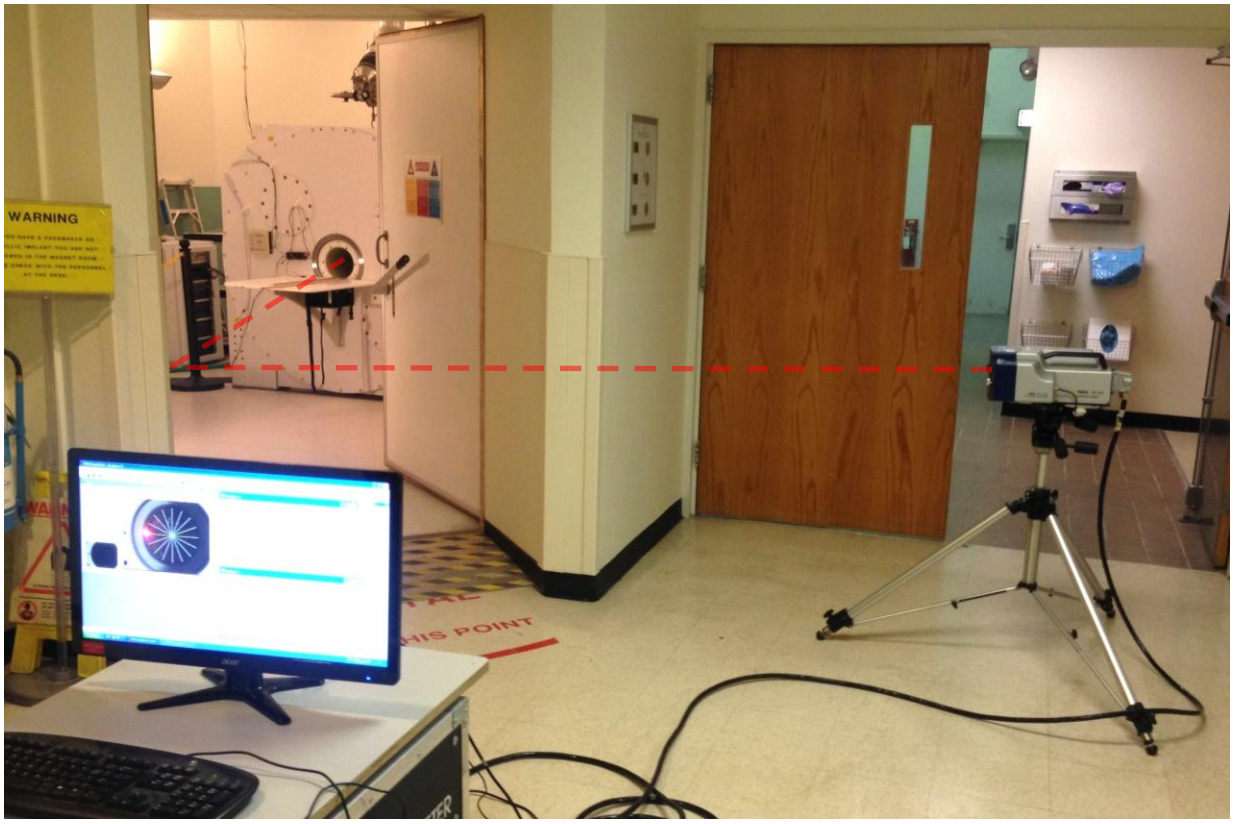

Figure 7-8: SLDV system set up for synchronous MRE and SLDV experiments.

Acknowledgments

This work was internally funded by the University of Illinois at Chicago Motion Sensitive MRI Lab

CHAPTER 8

CONCLUSIONS

The study in Chapter 4 investigated using MRE to measure internal pressure-induced changes in the wall shear stiffness of a cylindrical vessel with multiple tissue mimicking gel layers of different stiffness. Changes in the vessel wall shear stiffness values correlated with changes in gas and liquid pressure loading. Hysteresis was observed in the stiffness values as the pressure-induced stress was cycled. Our results indicate that MRE has the potential to serve as a noninvasive tool for the determination of pressure changes within biological tissue via measurement of surrounding tissue stiffness. The interconnected porosity phantom from Chapter 5 has promising experiential capabilities for investigating the influence of pore size on the pressure-MRE stiffness relationship.

Experimental investigations conducting tensile loading during MRE is fairly unexplored and may help to better understand tensile-dependent mechanical properties changes in relation to organ function. The tensile stress-strain relation in Chapter 6 resembled the Fung hyperelastic strain energy model. Observations conclude that MRE shear storage modulus is related to the state of tensile deformation. This study demonstrates the feasibility of simultaneous tensile testing during MRE and the new design can potentially be used for MRE calibration using pre-tension. The proposed tensile-MRE testing method may also serve as a useful experimental technique to explore parameter optimization methods for MRE calibration that are independent of time varying and temperature factors, and may therefore contribute to increase the accuracy of MRE.

Without declaring that one particular elastography method yields a gold standard for complex shear modulus, the study results in Chapter 7 support that MRE and OE are both precise since they show such similarities in displacement fields recorded at the same time while emanating from the same vibration source. The precision is also based on that the synchronously measured values of complex shear moduli are statistically not different while examining 3 independent controls in the study including

variations in frequency, stiffness, and testing material. The study confirms the reliability of using both MRI and SLDV as imagining modalities in elastography for assessing stiffness of soft tissue-mimicking media. Future studies should focus on a means to calibrate complex shear modulus to one standard value over all elastography methods. This will ultimately be necessary to use Elastography as a quantitative measure in disease progression related to changes in soft tissue stiffness. Investigations should also include using this platform to study the relationship between surface and internal wave propagation in inhomogeneous and anisotropic media under pre-stress from gas and liquid loading sources that simulate organ function.

CITED LITERATURE

Altaf A. Khan et al., 2013. LOCALIZED ELASTOGRAPHY MAP OF HUMAN CORNEA THROUGH SURFACE VIBRATIONS. In *Proceedings of the ASME 2013 International Mechanical Engineering Congress & Exposition*. pp. 1–4.

Arani, A., Plewes, D. & Chopra, R., 2011. Transurethral prostate magnetic resonance elastography: Prospective imaging requirements. *Magnetic Resonance in Medicine*, 65(2), pp.340–349.

Basford, J.R. et al., 2002. Evaluation of healthy and diseased muscle with magnetic resonance elastography. *Archives of Physical Medicine and Rehabilitation*, 83(11), pp.1530–1536.

Bloch, F., 1946. Bloch._Nuclear_Induction_1946_the_Equations. *Physical Review*, 70, p.460.

Chatelin, S., Constantinesco, A. & Willinger, R., 2010. Fifty years of brain tissue mechanical testing: From in vitro to in vivo investigations. *Biorheology*, 47(5-6), pp.255–276.

Chen, Q. et al., 2006. Differential effects of pre-tension on shear wave propagation in elastic media with different boundary conditions as measured by magnetic resonance elastography and finite element modeling. *Journal of Biomechanics*, 39(8), pp.1428–1434.

Chmarra, M.K. et al., 2013. Multimodal Phantom of Liver Tissue. *PLoS ONE*, 8(5), pp.1–9.

Clayton, E.H. et al., 2010. Comparison of Dynamic Mechanical Testing and MR Elastography of Biomaterials Department of Biomedical Engineering. , 4, pp.143–150.

Dresner, M. a et al., 2001. Magnetic resonance elastography of skeletal muscle. *J. Magn. Reson. Imaging*, 13, pp.269–276.

Ehman, R.L., Glaser, K.J. & Manduca, A., 2012. Review of MR elastography applications and recent developments. *Journal of Magnetic Resonance Imaging*, 36(4), pp.757–774.

Elgeti, T. et al., 2012. Vibration-synchronized magnetic resonance imaging for the detection of myocardial elasticity changes. *Magnetic Resonance in Medicine*, 67(4), pp.919–924.

Franculli, C., 2013. Mechanical and Calorimetric Characterization of Novel Environmentally Friendly Copolymers. In p. 43.

Fung, Y., Fronek, K. & Patitucci, P., 1979. Pseudoelasticity of arteries and the choice of its mathematical expression. *Am J Physiol.*, 237(5), pp.H620–31.

Fung YC, 1967. Elasticity of soft tissues in simple elongation. *Am J Physiol.*, 213(6), pp.1532–44.

Gerlach, W. & Stern, O., 1922. Der experimentelle Nachweis der Richtungsquantelung im Magnetfeld. *Der experimentelle Nachweis der Richtungsquantelung im Magnetfeld*, 9(1), pp.349–352.

Hamhaber, U. et al., 2003. Comparison of Quantitative Shear Wave MR- Elastography With Mechanical Compression Tests. *Magn Reson Med*, 49, pp.71–77.

Hirano, T. et al., 1995. In situ x-ray CT under tensile loading using synchrotron radiation. *J. Mater Res.*, 10(2), pp.381–386.

CITED LITERATURE (continued)

Hirsch, S., Beyer, F., et al., 2013. Compression-sensitive magnetic resonance elastography. *Physics in Medicine & Biology*, 58.

Hirsch, S., Klatt, D., et al., 2013. In Vivo Measurement of Volumetric Strain in the Human Brain Induced by Arterial Pulsation and Harmonic Waves. , 683, pp.671–683.

Hirsch, S., Posnansky, O., et al., 2013. Measurement of vibration-induced volumetric strain in the human lung. *Magnetic Resonance in Medicine*, 69(3), pp.667–674.

Hirsch, S. et al., 2014. Towards compression-sensitive magnetic resonance elastography of the liver: Sensitivity of harmonic volumetric strain to portal hypertension. *Journal of Magnetic Resonance Imaging*, 39(2), pp.298–306.

Kearney, S.P. et al., 2015. Dynamic viscoelastic models of human skin using optical elastography. *Physics in Medicine & Biology*, 60, p.6975. Available at: http://dx.doi.org/10.1088/0031-9155/60/17/6975.

Klatt, D. et al., 2013. Sample interval modulation for the simultaneous acquisition of displacement vector data in magnetic resonance elastography : theory and application. *Physics in Medicine and Biology*, 58(24), pp.8663–75.

Klatt, D., Friedrich, C., et al., 2010. Viscoelastic properties of liver measured by oscillatory rheometry and multifrequency magnetic resonance elastography. *Biorheology*, 47, pp.133–141.

Klatt, D., Papazoglou, S., et al., 2010. Viscoelasticity-based MR elastography of skeletal muscle. *Physics in medicine and biology*, 55(21), pp.6445–6459.

Kolipaka, A. et al., 2009. Evaluation of a rapid, multiphase MRE sequence in a heart-simulating phantom. *Magnetic Resonance in Medicine*, 62(3), pp.691–698.

Kolipaka, A. et al., 2012. Magnetic resonance elastography as a method to estimate myocardial contractility. *Journal of Magnetic Resonance Imaging*, 36(1), pp.120–127.

Larmor, J., 1896. The Influence of a Magnetic Field on Radiation Frequency. *Philosophical transactions of the Royal Society of London*, 60, pp.514–515.

Laubertur, P.C., 1973. Image formation by induced local interactions. *Nature*, 242, pp.190–191.

Leclerc, G.E. et al., 2012. Characterization of a hyper-viscoelastic phantom mimicking biological soft tissue using an abdominal pneumatic driver with magnetic resonance elastography (MRE). *Journal of Biomechanics*, 45(6), pp.952–957.

Lewa, C., 1991. Magnetic resonance imaging in the presence of mechanical waves. *Spectrosc. Lett.*, 24, pp.55–67.

Liu, Y. et al., 2016. Cardiac MR Elastography of the Mouse : Initial Results. *Magn Reson Med*.

Liu, Y., Yasar, T.K. & Royston, T.J., 2014. Ultra wideband (0.5–16 kHz) MR elastography for robust shear viscoelasticity model identification. *Physics in Medicine and Biology*, 59(24), pp.7717–7734.

CITED LITERATURE (continued)

Miller, K., 2001. How to test very soft biological tissues in extension? *J Biomech*, 34, pp.651–657.

Muthupillai, R. et al., 1995. Magnetic Resonance Elastogrphy by Direct Visualization of Propagating Acoustic Strain Waves. *Science*, 269, pp.1854–7.

Oudry, J., Chen, J., et al., 2009. Cross-validation of magnetic resonance elastography and ultrasound-based transient elastography: A preliminary phantom study. *Journal of Magnetic Resonance Imaging*, 30(5), pp.1145–1150.

Oudry, J., Vappou, J., et al., 2009. Ultrasound-based transient elastography compared to magnetic resonance elastography in soft tissue-mimicking gels. *Physics in medicine and biology*, 54, pp.6979–6990.

Paterson, M.S., 1964. Effect of Pressure on Young ' s Modulus and the Glass Transition in Rubbers Effect of Pressure on Young ' s Modulus and the Glass Transition in Rubbers. , 35(1).

Peng, Y. et al., 2014. Sound transmission in the chest under surface excitation: an experimental and computational study with diagnostic applications. *Medical & Biological Engineering & Computing*, pp.695–706.

Perri, P.R. et al., 2009. Modeling of Soft Poroelastic Tissue in Time-Harmonic MR Elastography. , 56(3), pp.598–608.

Perrinez, P.R. et al., 2010. Magnetic resonance poroelastography: An algorithm for estimating the mechanical properties of fluid-saturated soft tissues. *IEEE Transactions on Medical Imaging*, 29(3), pp.746–755.

Pickup, B.A. & Thomson, S.L., 2010. Flow-induced vibratory response of idealized versus magnetic resonance imaging- based synthetic vocal fold models. *J. Acoust. Soc. Am.*, 128(3), pp.124–129.

Rabi, I., Kellogg, J. & Zacharias, J., 1934. The magnetic moment of the proton. *Physical Review*, 46, pp.157–163.

Rajagopal, K.R., 2009. The mechanics and mathematics of the effect of pressure on the shear modulus of elastomers. , (August), pp.3859–3874.

Rashid, B., Destrade, M. & Gilchrist, M.D., 2014. Mechanical characterization of brain tissue in tension at dynamic strain rates. *Journal of the mechanical behavior of biomedical materials*, 33, pp.43–54.

Ringleb, S.I. et al., 2005. Quantitative Shear Wave Magnetic Resonance Elastography : Comparison to a Dynamic Shear Material Test. *Magn Reson Med*, 1201, pp.1197–1201.

Royston, T.J. et al., 2011. Estimating material viscoelastic properties based on surface wave measurements: A comparison of techniques and modeling assumptions. *The Journal of the Acoustical Society of America*, 130(6), p.4126.

Sack, I. et al., 2013. Structure-sensitive elastography: on the viscoelastic powerlaw behavior of in vivo human tissue in health and disease. *Soft Matter*, 9(24), p.5672. Available at: http://xlink.rsc.org/?DOI=c3sm50552a.

CITED LITERATURE (continued)

Salman, M. & Sabra, K.G., 2013. Surface wave measurements using a single continuously scanning laser Doppler vibrometer: application to elastography. *The Journal of the Acoustical Society of America*, 133(3), pp.1245–54. Available at: http://www.ncbi.nlm.nih.gov/pubmed/23463997.

Schwartz, B.L. et al., 2016. Axisymmetric diffraction of a cylindrical transverse wave by a viscoelastic spherical inclusion. *Journal of Sound and Vibration*, 364, pp.222–233. Available at: http://linkinghub.elsevier.com/retrieve/pii/S0022460X15009207.

Seber, G.A.F. & Wild, C.J., 2003. *Nonlinear Regression*, Hoboken, NJ: Hoboken, NJ : Wiley-Interscience.

Singhal, A. et al., 2013. Evolution of phase strains during tensile loading of bovine cortical bone. *Advanced Engineering Materials*, 15(4), pp.238–249.

Tabatabai, H. et al., 2013. Novel applications of laser doppler vibration measurements to medical imaging. *Sensing and Imaging*, 14(1-2), pp.13–28.

Tang, A. et al., 2015. Ultrasound elastography and MR elastography for assessing liver fibrosis: Part 2, diagnostic performance, confounders, and future directions. *American Journal of Roentgenology*, 205(1), pp.33–40.

Tse, Z.T.H. et al., 2009. Magnetic resonance elastography hardware design: a survey. *Proceedings of the Institution of Mechanical Engineers. Part H, Journal of engineering in medicine*, 223(4), pp.497–514. Available at: http://pih.sagepub.com/content/223/4/497.short\nhttp://pih.sagepub.com/content/223/4/497.abstract.

Uwe Hamhaber, Uwe Klose, Frieder Grieshaber, J.N., 2001. Evaluation of Quantitative MR-Elastography Measurements. *Proceedings of the International Society of Magnetic Resonance Imaging in Medicine (2001)*, (JANUARY 2001), p.1639.

Xie, H. et al., 2012. A phantom study to cross-validate multimodality shear wave elastography techniques. *IEEE International Ultrasonics Symposium, IUS*, pp.1858–1861.

Yasar, T.K., Royston, T.J. & Magin, R.L., 2013. Wideband MR elastography for viscoelasticity model identification. *Magn Reson Med*, 70(2), pp.479–489.

Yin, M. et al., 2013. Hepatic and Splenic Stiffness Augmentation Assessed With MR Elastography in an In Vivo Porcine Portal Hypertension Model. , 815, pp.809–815.

Yin, Z. et al., 2014. Mechanical Characterization of Tissue-Engineered. , 20(8), pp.611–619.

Yogesh K Mariappan, Kevin J Glaser, R.L.E., 2011. MAGNETIC RESONANCE ELASTOGRAPHY: A REVIEW. *Clinical anatomy*, 23(5), pp.497–511.

Zsch, H.E.T., 2015. MULTIFREQUENCY TIME-HARMONIC ELASTOGRAPHY FOR THE. , 41(3), pp.724–733.

VITA

EDUCATION:

Doctor of Philosophy in Mechanical Engineering, University of Illinois at Chicago, 2016

Bachelor of Science in Mechanical Engineering, Southern Illinois University Edwardsville, 2009

PUBLICATIONS, AWARDS, & CONFERENCE APPEARANCES*:*

MA Rossi, G Stebbins, C Murphy, D Greene, S Brinker, et al., Predicting white matter targets for direct neurostimulation therapy. Epilepsy Research, Volume 91, Issue 2 , Pages 176-186, October 2010

Kearney SP, Brinker ST, et al. SLIM-MRE without prolonged echo time for the simultaneous acquisition of the 3D displacement vector applied to in vivo mouse brain. ISMRM 23rd Annual Meeting

16th International Conference on Experimental Mechanics, Cambridge UK, July 7-11, 2014

National Aeronautics and Space Administration University Student Competition 2006, Honorable Mention for SIUE, "Quite House"

***ACADEMIC EXPERIENCE*:**

Preclinical 9.4 T MRI Facility at UIC Research Resources Center

Machinist and Scientific Instrument Maker and MRI Operator *May 2012 – Apr 2016*

Design and fabricate custom Magnetic Resonance Imaging equipment for medical research.

Operate and manage machinery in MRI machining facility.

Maintenance and operate preclinical 9.4 T MRI imaging system (perform magnetic resonance elastography experiments).

Perform Matlab image processing, write animal research protocols and facility standard operating procedures.

Acoustics and Vibrations Laboratory

Research Assistant *Oct 2011 - Apr 2012*

Primary responsibility was to build and test piezoelectric systems for Magnetic Resonance Elastography.

Operate Scanning Laser Doppler Vibrometry System (PSV-400 Polytec Inc).

VITA (continued)

Design and build radio frequency coils for small MRI probes.

Engineering Design and Decision Laboratory

Engineering Graduate Assistant *Jul 2010 to Sep 2011*

Operate and maintenance rapid prototyping 3D printing systems.

Provide engineering support for airport tarmac vehicle designs.

Epilepsy Center at Rush University Medical Center

Research Engineer
Summer 2008

Develop modeling system for strategically placed human brain depth electrode implantation.

Accompany principal investigator in Food and Drug Administration trial meetings for Responsive Neurostimulator device (NeuroPace Inc).

Model depth electrodes in MRI generated brain geometries using FEM COMSOL Multiphysics.

Accompany physician and brain surgeon in patient trial evaluation appointments, implantation process including surgery, and device effectiveness in patient follow-up activities.

INDUSTRY EXPERIENCE:

Citgo Petroleum Corporation

Reliably Engineer *Aug 2013 – Apr 2015*

(contracted by Priority Staffing, Ltd.)

Worked in reliability engineering at Citgo Lemont Refinery in support of static equipment maintenance**.**

Responsible for Fluid Catalytic Cracking reliably issues such as boilers and petroleum processing systems**.**

Conducted field observations on damaged systems in refinery on request of engineering management**.**

Project management of environmental probe assemblies repairs for company continuous improvement goals.

VITA (continued)

ConocoPhillips Wood River Refinery

Construction Engineer / Coordinator *Feb 2009 - Nov 2009*

(contracted by Administrative Exchange, INC.)

Primary responsibility was overseeing the work of engineering and construction contractors for compliance with company standards and project contracts.

Project management and coordination of critical crane lifts and heavy hauls.

Design and implement rigging plans and permits for critical crane lifts.

United States Steel Corporation

Metallurgy Engineer Intern *May 2007 - Oct 2007*

Worked in steel making department, basic oxygen furnace and continuous casters.

Assist metallurgists and operation managers.

Conduct efficiency studies, vessel emissions, plant mapping.